CANE1-mediated autophagosome size regulation fine-tunes phosphate starvation tolerance in *Arabidopsis thaliana*

David Görg[1], Fiona Smith[1], Klara Machalett[1,2], Falko Koblenz[1], Ymy Thi Ngo[1], Sascha Höhne[1], Julian Arndt[1], Sylvestre Marillonnet[3], Nenad Grujic[4], Richard Imre[4,5], Karl Mechtler[4,5], Yasin Dagdas[6], and Christin Naumann[1*]

[1]Department of Molecular Signal Processing, Leibniz Institute of Plant Biochemistry, 06120 Halle (Saale), Germany

[2]Institute of Biochemistry and Biotechnology, Martin Luther University Halle-Wittenberg, Halle (Saale), Germany

[3]Department of Cell and Metabolic Biology, Leibniz Institute of Plant Biochemistry, 06120 Halle (Saale), Germany

[4]Gregor Mendel Institute of Molecular Plant Biology, Vienna, Austria

[5]Research Institute of Molecular Pathology (IMP), Vienna BioCenter (VBC), Vienna, Austria

[6]Heidelberg University, Centre for Organismal Studies, Heidelberg, Germany

*****Corresponding author e-mail: cnaumann@ipb-halle.de

ORCID IDs: 0000-0002-9712-5728 (D.G.); 0009-0004-4740-3197 (K.M.); 0000-0002-4263-797X (S.M.); 0000-0002-9502-355X (Y.D.); 0000-0001-6972-155X (C.N.)

ABSTRACT

Inorganic phosphate (Pi) availability determines root development and plant performance. In *Arabidopsis thaliana*, external Pi is sensed by root tips and Pi limitation triggers ER stress–induced autophagy, yet the physiological impact and mechanisms controlling autophagosome biogenesis remain unclear. Here, we identify CANE1 (COMPONENT OF AUTOPHAGIC NETWORK) as a novel plant-specific regulator of autophagosome size in local Pi sensing. CANE1 associates with the plasma membrane-ER tethering protein VAP27-1 and binds to Pi-responsive ATG8 isoforms through conserved interaction motifs. Loss of CANE1 augments ER stress resistance by reducing autophagosome size in Pi-deprived root tips. Our findings establish CANE1 as a determinant of autophagosome size at the ER membrane. Thus, CANE1 functions as a molecular link between Pi-dependent ER stress signaling and fine-tuning of autophagic capacity.

33 **INTRODUCTION**

34 Plant growth and development are tightly constrained by nutrient availability in soil.
35 Phosphorus, primarily absorbed as inorganic phosphate (Pi), is the second most critical
36 macronutrient, and Pi availability is often limited by complex chemical interactions with
37 associated metals (e.g. Fe, Al) (Abel 2017; Abel and Naumann 2024; Lambers et al. 2015;
38 Shen et al. 2011). To enhance Pi acquisition for maintaining cellular Pi homeostasis, plants
39 undergo extensive developmental and metabolic reprogramming, which includes remodeling
40 of root system architecture and chemical modification of the rhizosphere, respectively
41 (Crombez et al. 2019; Giehl and von Wiren 2014; Kellermeier et al. 2014; Yang et al. 2024).
42 In growing root tips of *Arabidopsis thaliana*, low external Pi rapidly reduces cell elongation
43 and progressively inhibits cell division (Balzergue et al. 2017; Clua et al. 2024; Maniero et al.
44 2024; Muller et al. 2015; Naumann et al. 2022). The single ER-resident P5A-type ATPase
45 PHOSPHATE DEFICIENCY RESPONSE 2 (PDR2) and the apoplastic ferroxidase LOW
46 PHOSPHATE ROOT 1 (LPR1) form the core module of local Pi sensing in root tips
47 (Svistoonoff et al. 2007; Ticconi et al. 2001; Ticconi et al. 2009). Decreasing Pi-availability
48 activates LPR1 by facilitating access to its substrate (Fe^{2+}), triggering cell-type-specific Fe^{3+}
49 accumulation, formation of reactive oxygen species (ROS), and cell wall modifications,
50 which interrupts cellular communication and consequently root growth (Balzergue et al. 2017;
51 Gutierrez-Alanis et al. 2017; Muller et al. 2015; Naumann et al. 2022). PDR2 counteracts
52 LPR1 function by maintaining root tip Fe homeostasis through an unknown mechanism
53 (Jakobsen et al. 2005; Muller et al. 2015; Naumann et al. 2022; Naumann et al. 2019; Ticconi
54 et al. 2009). Biochemical and structural studies reveal that P5A-type ATPases (P5As) act as
55 membrane-helix dislocases that assist transmembrane protein insertion and remove
56 mistargeted proteins, thereby safeguarding ER function and organelle integrity (Ji et al. 2024;
57 Li et al. 2024; McKenna et al. 2022; McKenna et al. 2020). Disruption of P5A activity is
58 detrimental across eukaryotes, affecting neuronal development in animals and causing

59 pleiotropic ER-associated defects in yeast (Feng et al. 2020; Li et al. 2021; Qin et al. 2020;
60 Sim and Park 2023). In plants, PDR2 function in root tips is linked to Pi-dependent ER stress-
61 induced autophagy (Naumann et al. 2019; Stephani et al. 2020; Ticconi et al. 2009).
62 Autophagy is a conserved degradation pathway essential for protein and organelle quality
63 control, cellular homeostasis, and stress adaptation (Gross et al. 2025; Liu and Bassham 2012;
64 Petersen et al. 2024; Su et al. 2020). Damaged organelles or protein aggregates are
65 sequestered into double-membrane autophagosomes, typically 0.5–1.5 μm in diameter, which
66 subsequently fuse with the vacuole for cargo degradation (Nakatogawa 2020; Zhao et al.
67 2022; Zheng et al. 2018). Autophagosome biogenesis originates at ER-associated phagophore
68 initiation sites through PI3K complex (ATG6–VPS15–VPS34–ATG14) recruitment and
69 progresses via ATG8 lipidation, mediated by the ATG12–ATG5–ATG16 complex.
70 Additional regulators, such as SH3P2, interact with ATG8 and the PI3K complex to support
71 phagophore expansion, cargo loading, vacuolar targeting, and possibly autophagosome size
72 control (Nascimbeni et al. 2017; Walczak and Martens 2013; Zhuang et al. 2013). Selective
73 autophagy receptors, including NBR1 (Jung et al. 2020; Svenning et al. 2011) and C53
74 (Stephani et al. 2020), deliver defined cargos to the phagophore through ATG8 interaction
75 motifs (AIMs), and cargo characteristics can directly influence autophagosome dimension
76 (Johansen and Lamark 2020). ATG8 isoforms enable organ- and stress-specific autophagy
77 responses as illustrated by the differential complementation of carbon and nitrogen starvation
78 phenotypes (Del Chiaro et al. 2025; Dong et al. 2025; Liu et al. 2021; Thompson et al. 2005).
79 Beyond nutrient starvation, local Pi sensing in root tips and Pi deficiency in green tissues
80 triggers iron-mediated ER stress-induced autophagy, likely originating from cargo overload
81 within the secretory pathway (Naumann et al. 2019; Yoshitake et al. 2022). Notably,
82 autophagosome size is highly variable and strongly shaped by the nature of the target, yet how
83 autophagosome dimensions are controlled during biogenesis remains unknown. Emerging
84 evidence suggests that ER-associated proteins at phagophore initiation sites are likely central

85 to autophagosome size determination; however, the molecular mechanism and components
86 involved remain elusive.
87
88 Here, using quantitative proteomics and interaction assays in Arabidopsis, we report a novel
89 COMPONENT OF THE AUTOPHAGIC NETWORK (CANE1) as a plant-specific regulator
90 of autophagosome size during Pi limitation. CANE1 associates with the ER–plasma
91 membrane tethering protein VAP27-1 and the ER-membrane embedded glycosylation
92 complex component DGL1, interacts with root tip-localized ATG8B and ATG8C isoforms
93 via conserved AIM motifs, and its loss of function results in smaller autophagosomes and
94 enhanced ER stress resistance. Through its role in Pi-mediated autophagy, CANE1 shapes
95 autophagosome biogenesis, establishing an ER-associated regulatory network that converges
96 with ATG8-mediated, organ-specific autophagy.
97
98 **RESULTS**
99 **Phosphate limitation induces ATG8 isoform specific ER stress mediated autophagy**
100 Tissue specific expression of ATG8 isoforms (ATG8A-ATG8I) in *Arabidopsis thaliana*
101 mediate the autophagic response under distinct stress conditions (Del Chiaro et al. 2025;
102 Dong et al. 2025). To investigate their roles in local root Pi sensing, we monitored native
103 promoter-driven GFP-ATG8 protein fusions (*pATG8x::GFP-ATG8x*) (Del Chiaro et al. 2025)
104 for autophagosome formation in wildtype (WT) seedlings transferred from Pi-replete (+Pi) to
105 Pi-deprived (-Pi) conditions as well as after exposure to carbon starvation (-C) and
106 tunicamycin-induced (+TM) ER stress (Fig. S1). Consistent with previous reports, GFP
107 fluorescence was largely absent in basal (+Pi) condition for most ATG8 isoforms with the
108 exception of ATG8A and ATG8F (Del Chiaro et al. 2025; Dong et al. 2025; Thompson et al.
109 2005). Upon carbon starvation, all tested lines exhibited GFP-positive puncta formation in the
110 root transition zone and, to a lower extent, in the root tip, indicative of bulk autophagy

111 activation independent of isoform specificity (Fig. S1). Likewise, TM treatment induced
112 autophagosome formation in the transition zone of all transgenic GFP-ATG8 lines. Notably,
113 Pi deprivation selectively activated autophagosome formation in root tips expressing GFP-
114 ATG8 fusion isoforms B, C, and E suggesting an ATG8 isoform-specific involvement in Pi
115 sensing (Fig. 1a, Fig. S1). Given that local root Pi sensing triggers ER stress-mediated
116 autophagy in Pi limitation via the PDR2–LPR1 module (Naumann et al. 2019; Stephani et al.
117 2020), we introgressed *pATG8B/C::GFP-ATG8B/C* transgenes into the Pi-sensitive
118 *pdr2* mutant and monitored autophagosome formation following Pi deprivation. When
119 compared to +Pi conditions, the number of GFP-ATG8B labelled autophagosomes increased
120 2-fold and 2.5-fold in wildtype and *pdr2* roots, respectively, with no significant changes in
121 *ATG8* transcript levels (Fig. 1, Fig. S2a). Interestingly, the number of GFP-ATG8C labelled
122 puncta increased significantly only in *pdr2,* suggesting a specific role in ER quality control,
123 which is supported by enhanced autophagosome formation upon TM treatment (Fig. 1).
124 To assess ATG8 isoform-specific functionality, we examined local Pi sensing in the ATG8-
125 deficient nonuple mutant *Δatg8* (Del Chiaro et al. 2025), alongside complementation lines
126 expressing GFP-ATG8A or GFP-ATG8H, representing the two major ATG8 clades in
127 *Arabidopsis* (Rogov et al. 2023). *Δatg8* mutants exhibited modest root growth defects in Pi
128 deprivation, indicative of enhanced ER stress sensitivity (Fig. S2b). Notably, ectopic
129 expression of either ATG8A or ATG8H did not rescue this phenotype, implying that
130 autophagosome induction in local Pi sensing may involve isoform-specific functions.

131 **Local Pi sensing remodels autophagy-dependent root tip proteome**

132 To elucidate the biological role of ER stress-induced autophagy in local Pi sensing and
133 uncover novel components, we employed two complementary mass spectrometry-based
134 screening approaches. Our working hypothesis posits that proteins regulated in an autophagy-
135 dependent mode during Pi sensing should (i) exhibit altered abundances in autophagy-
136 deficient mutants such as *atg2*, and (ii) physically interact with ATG8 isoforms. First, we

137 performed proteomic profiling of wildtype, *pdr2*, and *atg2* root tips using tandem mass tag-
138 based quantitative mass spectrometry (TMT-MS). Seedlings were germinated in Pi-
139 sufficiency and subsequently transferred to control (+Pi) or ER stress-inducing (−Pi or +TM)
140 conditions. Comparative analysis revealed that either ER stress condition caused pronounced
141 proteomic shifts in root tips, with *atg2* displaying a significantly higher number of
142 differentially abundant proteins relative to wildtype and *pdr2* (Fig. 2a, Fig. S3a, Data S1). We
143 next analyzed the protein abundances in ER stress conditions in *atg2* in comparison to WT or
144 *pdr2*. For Pi-deprivation 89 proteins were increased in *atg2* but not in wildtype or *pdr2* root
145 tips, suggesting autophagy-dependent regulation (Fig.2b, Fig. S3b). This set includes core
146 autophagy components such as ATG4, multiple ATG8 isoforms, and selective autophagy
147 receptors, NBR1 and C53, previously implicated in ER stress responses and Pi signaling
148 (Picchianti et al. 2023; Stephani et al. 2021; Stephani et al. 2020; Wild et al. 2014).
149 Enrichment of these proteins reinforced the validity of our experimental design and highlights
150 a functional role of autophagy in maintaining proteostasis during local Pi perception.
151 Second, to identify Pi-responsive ATG8 interactors, we performed immunoprecipitation
152 coupled with mass spectrometry (IP-MS) using wildtype and *pdr2* lines expressing
153 *p35S::GFP-ATG8A* (Fig. S3d, e; Data S2). This screen revealed over 300 potential
154 interactors, including ATG8B and ATG8C as well as NBR1 and C53, which are established
155 ATG8 interactors (Stephani et al. 2020; Wilfling et al. 2020; Zhao et al. 2022).
156 To discover functionally relevant ATG8-associated proteins in Pi-deprivation, we cross-
157 referenced the ATG8A interactome (Fig. 2c,d) with the set of 89 proteins stabilized in *atg2*
158 (Fig. 2b), which revealed ATG8B, ATG8C, NBR1 and an uncharacterized protein
159 (AT5G40690), among the most enriched candidates across both datasets (Fig. 2e). Consistent
160 detection of AT5G40690, suggests a novel function in autophagy-dependent Pi sensing and
161 root proteostasis. We therefore refer to AT5G40690 as CANE1 (COMPONENT OF
162 AUTOPHAGIC NETWORK).

163 **CANE1 is evolutionally conserved among land plant species**

164 While the core autophagy machinery is conserved across plants, the identification of
165 modulators fine-tuning the autophagic pathway remains an active area of investigation
166 (Cadena-Ramos and De-la-Pena 2024; Gross et al. 2025; Stephani and Dagdas 2020).
167 AT5G40690 encodes a small, 210-amino-acid protein, expressed from a single exon.
168 Phylogenetic analysis revealed that CANE1 is exclusive to and conserved across mostly all
169 major land plant lineages apart from ferns and gymnosperms (Fig. 3a, Fig. S4).
170 Notably, in a subset of angiosperms, including both monocot and dicot species but not
171 bryophytes and *Amborella trichopoda*, we identified additional gene homologs encoding
172 truncated proteins (~110 amino acid residues), that lack the C-terminal domain present in
173 canonical CANE1 orthologs (Fig. 3a, Fig. S4). In Arabidopsis, two such paralogs, HRG1
174 (AT2G411730) and HRG2 (AT5G24640) have been implicated in reactive oxygen species
175 (ROS)-mediated root meristem maintenance (Gong et al. 2021). These findings suggest
176 functional divergence or neofunctionalization of HRG proteins within specific angiosperm
177 lineages such as the Brassicaceae.
178 Expression analysis in whole seedlings revealed consistent upregulation of *CANE1* transcript
179 levels in autophagy-deficient mutants (*atg2*, *atg5*, *atg7*, and *atg9*) compared to the wildtype
180 control (Fig. 3b). To investigate organ- and tissue-specific *CANE1* expression, we generated
181 transgenic *pCANE1::GUS* wildtype and *atg5* mutant lines (Fig. 3b-d). In wildtype, *CANE1*
182 promoter activity was predominantly detected in root tissues, including lateral roots and root
183 hairs, with increased activity in the root-shoot junction, while only weak GUS reporter signals
184 were observed in the tip region of cotyledons and true leaves as well as in flowers and
185 developing siliques (Fig. 3b,c). Interestingly, in the *atg5* background, the spatial distribution
186 of *CANE1* promoter activity was comparable to wildtype, but markedly enhanced as
187 evidenced by intense GUS staining, which correlates to elevated *CANE1* transcript levels
188 measured in autophagy-deficient lines (Fig. 3b, d). Collectively, the evolutionary conservation

189 of *CANE1*, its dominant expression in roots, and its transcriptional activation in autophagy
190 mutants support a role for *CANE1* in nutrient-dependent ER stress responses in land plants.

191 **CANE1 interacts with ATG8 in an AIM-dependent manner**

192 Co-immunoprecipitation of endogenous ATG8 with CANE1-mCherry expressed in
193 Arabidopsis roots experiencing ER stress (Fig. 4a) validated our initial IP-MS identification
194 of CANE1 as an ATG8 interactor (Fig. 2). We combined structural modeling with *in vitro* and
195 *in vivo* studies to determine the ATG8-binding site of CANE1. AlphaFold2 modelling
196 indicated CANE1 to be intrinsically disordered and predicted the presence of five putative
197 ATG8-interacting motif (AIM) consensus sequences (W/F/V-X-X-L/I/V), with AIM5 (aa
198 202-205) being the best candidate followed by AIM4 (aa 183-189) (Fig. 4b; Fig. S5). Yeast
199 two-hybrid interaction assays indicated AIM5-dependent CANE1 binding to all ATG8
200 isoforms, and strong interaction with ATG8G, H, and I (Fig. 4c). Transient expression of GFP
201 fusions of CANE1 in tobacco (*Nicotiana benthamiana*) and live cell imaging showed
202 predominantly cytosolic localization with partial net-like association reminiscent of ER
203 structures (Fig. 4d). Importantly, the subcellular localization observed for GFP-CANE1 was
204 not altered by introducing AIM4 and/or AIM5 deletions (Fig. 4e). Subsequent co-
205 immunoprecipitation analysis demonstrated the dominant role of AIM5 in CANE1 for ATG8
206 binding. While GFP-CANE1 interacted with all RFP-ATG8 isoforms in tobacco leave
207 extracts, which was also true for GFP-CANE1$^{\Delta AIM4}$, deletion of AIM5 (GFP-CANE1$^{\Delta AIM5}$)
208 abrogated CANE1 interaction with most ATG8 isoforms except for ATG8E and ATG8G. As
209 expected, deletion of AIM4 and AIM5 abolished CANE1$^{\Delta AIM4/5}$ binding to any ATG8 isoform
210 (Fig. 4f; Fig. S6). Collectively, our results demonstrate differential interaction of CANE1 with
211 ATG8 isoforms, which is primarily mediated by AIM5.

212 **CANE1 functions in ER stress-dependent autophagy during local Pi sensing**

213 To investigate the relevance of CANE1–ATG8 interaction *in vivo* and its role for root
214 responses to ER stress, we monitored autophagosome formation in transgenic lines expressing

215 GFP-tagged CANE1 (*pCANE1::CANE1-GFP; pUBQ10::GFP-CANE1*) (Fig. 5a-d, Fig. S7).
216 Consistent with transient expression in tobacco (Fig. 4d, e), CANE1-GFP exhibited a diffuse
217 cytoplasmic distribution under control conditions, occasionally forming low-intensity puncta,
218 which remained unchanged when expressed in the low Pi-sensitive *pdr2* mutant (Fig. 5a, Fig.
219 S7a ,c).
220 Induction of ER stress by low Pi or TM treatment caused a rapid and robust increase in
221 CANE1-GFP puncta and partial net-like localization with further enhancement in *pdr2* root
222 cells (Fig. 5a,b). Importantly, CANE1 transcript levels and spatial expression in root tips
223 remained unaffected in all lines tested (Fig. S7e,f). CANE1-GFP puncta co-localized with
224 mCherry-ATG8E, demonstrating CANE1 association with autophagosomes (Fig. 5c,d, Fig.
225 S7; (Feng et al. 2022)). Consistently, no CANE1-GFP puncta were detected in the autophagy-
226 deficient *atg5* mutant although basal CANE1-GFP protein abundance was increased in *atg2*
227 and *atg5* (Fig. S8d). These findings demonstrate that CANE1 associates with the ER and
228 autophagosomes during ER stress in root tips, with a more pronounced response under Pi
229 limitation compared to pharmacological ER stress induction by TM (Fig. 5a–d).
230 To investigate CANE1 function in *Arabidopsis*, we first analyzed T-DNA insertion (3'UTR)
231 line (*SALK_092190*), which does not affect transcript abundance (Fig. S8a, b). We then
232 generated two independent loss-of-function alleles using CRISPR–Cas9-mediated genome
233 editing (Stuttmann et al. 2021): *cane1-c1*, carrying an insertion resulting in a frameshift and
234 premature stop codon, and *cane1-c3*, harboring a deletion predicted to have a similar effect
235 (Fig. S8b-c). Both mutant lines were phenotypically indistinguishable from wildtype during
236 germination and early root development (Fig. 5e, f). Under ER stress conditions, however,
237 both *cane1* loss-of-function alleles exhibited increased survival on TM-containing medium,
238 indicating enhanced resistance (Fig. 5e). By contrast, no phenotypic differences were
239 observed under carbon or nitrogen starvation, a condition commonly used to activate bulk
240 autophagy (Fig. S8f-h).

241 We next examined the role of CANE1 in local Pi sensing. While both *cane1* mutants were
242 significantly less sensitive to Pi deprivation, exhibiting enhanced primary root elongation,
243 *CANE1* overexpression (*pUBQ10::GFP-CANE1*) displayed the opposite root growth
244 phenotype on low Pi medium (Fig. 5f). However, the *CANE1* loss- and gain-of-function lines
245 tested were indistinguishable with respect to iron and callose accumulation in root tips, two
246 histochemical markers of local Pi sensing (Naumann et al. 2022) (Fig. S9).
247 Thus, our observations suggest that CANE1 is dispensable for bulk autophagy but functions
248 in ER stress-induced autophagy modulating root growth response under local Pi limitation.
249 **CANE1 facilitates autophagosome biogenesis through ER tethering with VAP27-1**
250 To elucidate a role of CANE1 in autophagy, we analysed the CANE1 interactome under basal
251 and ER stress conditions. Under ER stress, CANE1 associates with ATG8C and factors
252 involved in autophagosome maturation (ATG3, FREE1, SH3P2, VPS34, NBR1) and the ER
253 membrane (VAP27-1, DGL1), implicating CANE1 function in phagophore expansion
254 (Fig. 6a; Fig. S10a). Co-immunoprecipitation confirmed CANE1 interaction with NBR1 in
255 wildtype and *atg5* roots, restricted to ER stress in wildtype and stabilized by ConA treatment
256 (Fig. 6b). Considering the CANE1 localization and interactome under stress (Fig. 5c, Fig. 6a,
257 Fig. S10a), we tested interactions of CANE1 with DGL1, an ER quality control component of
258 the OST complex (Lerouxel et al. 2005), and with VAP27-1, an ER–PM tether involved in
259 endocytosis and mitophagy (Li et al. 2022; Man et al. 2024; Stefano et al. 2018; Wang et al.
260 2019). CANE1 co-immunoprecipitated with DGL1 (Fig. S10b), supporting ER recruitment of
261 CANE1. VAP27-1 also interacted with CANE1 in tobacco leaves and Arabidopsis roots
262 under Pi limitation or TM-induced ER stress (Fig. 6c,d), suggesting that CANE1 may anchor
263 phagophores to the ER via VAP27-1 interaction and, enable autophagosome membrane
264 expansion. Notably, GFP-ATG8A puncta were smaller in *cane1-c1* root tips under Pi
265 limitation, while NBR1 turnover and autophagosome amount remained unaffected (Fig. 6e,f,

266 Fig. S10d, e), consistent with impaired phagophore expansion. CANE1 protein abundance
267 remained unchanged in ER stress (Fig. S8e, S10c).

268 **DISCUSSION**

269 Autophagy is essential for plant stress adaptation by maintaining cellular homeostasis under
270 fluctuating environmental conditions, yet the mechanisms determining autophagosome
271 maturation and size are largely unknown (Gross et al. 2025; Nakatogawa 2020; Zhao et al.
272 2022). In Arabidopsis, sensing of Pi limitation provokes iron-dependent ER stress response
273 followed by selective autophagy induction in growing root tips and photosynthetic tissues;
274 however the molecular determinants involved remain to be elucidated (Naumann et al. 2019;
275 Yoshitake et al. 2021; Yoshitake et al. 2022). Here we identify CANE1 as a novel
276 plant-specific regulator of autophagosome size during local root tip Pi-sensing. CANE1
277 associates with the ER through interaction with VAP27-1 and the OST complex subunit
278 DGL1, which is essential for ER protein quality control (Lerouxel et al. 2005) (Fig. 6).
279 Following ER stress perception, CANE1 associates with Pi-responsive ATG8 isoforms (B and
280 C) preferentially via its C-terminal AIM motif (Fig. 1, 4). Loss of CANE1 leads to significant
281 smaller autophagosomes and enhanced ER stress resistance (Fig. 5, 6) positioning CANE1
282 function in Pi-dependent ER stress signaling to the regulation of autophagosome biogenesis
283 and maturation.

284 Phagophore expansion occurs at ER-associated initiation sites where lipid flux, membrane
285 moulding, and cargo capture are coordinated (Gross et al. 2025; Liu et al. 2020; Liu and
286 Bassham 2012; Nascimbeni et al. 2017; Su et al. 2020; Zhuang et al. 2013). The ER–PM
287 tethering protein VAP27-1 is a key organizer of ER contact sites and supports mitophagy by
288 promoting ER-mitochondria connections necessary for phagophore expansion around
289 dysfunctional mitochondria (Li et al. 2022; Wang et al. 2019). VAP27-1 and its yeast
290 homologues further support ER-stress adaptation through interactions with soluble ER-phagy
291 receptors (Nthiga et al. 2020; Zhao et al. 2020). Although loss of VAP27-1 or DGL1 severely

292 compromises plant development due to their essential roles in membrane tethering and
293 N-glycosylation (Lerouxel et al. 2005; Wang et al. 2016), loss of CANE1 results instead in
294 enhanced ER stress resistance, indicating a more specialized function. The interaction of
295 CANE1 with VAP27-1 and DGL1 (Fig. 6) suggests that CANE1 contributes to stabilizing
296 phagophore–ER contacts, a process central to the controlled expansion of the autophagosome
297 membrane. We propose CANE1 modulates phagophore elongation by reinforcing ER–
298 membrane interfaces via VAP27-1 and acts together with Pi-responsive ATG8B/C isoforms
299 to establish a root cell-specific expansion regime for controlling autophagosome size. Such a
300 CANE1–VAP27-1–ATG8B/C complex may further provide the spatial framework necessary
301 for PI3K complex recruitment, thereby coordinating phagophore growth with cargo
302 encapsulation.
303 In the physiological context of growing root tips, the degradation of stress-induced cargo must
304 be balanced with the preservation of resources, especially under limited Pi availability. The
305 smaller autophagosomes observed in *cane1* likely favour rapid turnover of small or diffusible
306 cargos during early ER stress perception via the LPR1-PDR2 module, conferring enhanced
307 resistance to low-Pi stress. Conversely, CANE1-dependent enlargement of autophagosomes
308 in wildtype may facilitate more efficient sequestration of larger, bulky cargo, albeit at reduced
309 throughput. This size-throughput trade-off aligns with the gradual response of Pi–Fe-linked
310 ER stress induction, where rapid turnover may facilitate cell adaptation and sustain plant
311 survival (Naumann et al. 2022; Naumann et al. 2019). CANE1 probably functions separate of
312 established regulators of autophagosome maturation and fusion, such as SH3P2 and FREE1,
313 whose loss is lethal, as well as autophagy inhibitors including COST1 and Rubicon-related
314 factors (Bao et al., 2020; Gao et al., 2015; Matsunaga et al., 2009; Walczak & Martens, 2013;
315 Zhuang et al., 2013). This reveals CANE1 function at a previously unrecognized regulatory
316 layer dedicated specifically to autophagosome size determination.

317 We propose that in roots CANE1 relocates to ER contact sites upon low Pi stress, engaging
318 ATG8B/C and VAP27-1 to stabilize PI3P complexes and regulate phagophore elongation.
319 Following autophagosome closure, NBR1 may recruit CANE1 for turnover, positioning
320 CANE1 as a new local regulator of autophagosome expansion (Fig. 6g). Our findings
321 unravelled a complex regulatory network opening new avenues to dissect cargo selectivity
322 and stress-responsive remodelling of endomembrane systems for plant environmental
323 adaptation.
324
325

326 **METHODS**

327 **Plant Materials**

328 All *Arabidopsis thaliana* lines used in this study originate from accession Columbia (Col-0).
329 Mutant lines *pdr2-1 (Ticconi et al. 2009)*, *lpr1 lpr2* (Svistoonoff et al. 2007), *ire1a ire 1b*
330 (Naumann et al. 2019), *atg5-4 (Suzuki et al. 2005)*, *atg2-1* (Wang et al. 2011), *atg7-3* (Lai et
331 al. 2011), *atg9-4* (Shin et al. 2014), *Δatg8 (Del Chiaro et al. 2025)* and transgenic lines
332 *p35S::GFP-ATG8A* (Thompson et al. 2005), *pdr2-1 x p35S::GFP-ATG8A* (Naumann et al.
333 2019), *35Spro::SpER-GFP-HDEL, pdr2-1 x 35Spro::SpER-GFP-HDEL (Ticconi et al.*
334 *2009), pUBQ10::mCherry-ATG8E, atg5-1 x pUBQ10::mCherry-ATG8E* (Stephani et al.
335 2020), *Δatg8* x *pUBQ10::ATG8A*, *Δatg8* x *pUBQ10::ATG8H* (Del Chiaro et al. 2025) were
336 previously described. T-DNA insertion line SALK_092190 was obtained from the European
337 Arabidopsis Stock Center (NASC). The *cane1-c1* and *cane1-c3* knockout lines were produced
338 by CRISPR-Cas9 technology (Stuttmann et al. 2021). Guide RNAs for target sequences
339 (AAGCGTGAAGGCAAACAACAC and AACCCGGAAAGCTTCAAACC) were designed
340 with CHOPCHOP (Labun et al. 2019) and cloned into pDGE332_M1 and pDGE334_M2E
341 constructs (Ordon et al. 2017; Stuttmann et al. 2021) and assembled in pDGE347 for
342 transformation. Double mutants were generated by genetic crossing and genotyped by PCR.
343 Primers used for cloning and genotyping are listed in Supplementary table 1 and all vectors
344 are listed in Supplementary table 2.

345 **Molecular Cloning**

346 The *AtDGL1* coding sequence (CDS) was synthesized by Thermo Fisher Scientific with three
347 point mutations introduced to eliminate internal BpiI recognition sites. The CDS was flanked
348 by BpiI sites to enable Golden Gate cloning and subcloned into the MoClo vector
349 pAGM1287, generating the level 0 *AtDGL1* module pNAU7. The *Arabidopsis thaliana*
350 Ubiquitin 10 (Ubi10) promoter was amplified by PCR from plasmid pRedRoot (Limpens et
351 al. 2004) and cloned as MoClo level 0 promoter modules pAGM11323, flanked by BpiI sites

352 GGAG and AATG for use as a standard promoter module, and pAGM11335, flanked by BpiI
353 sites GGAG and CCAT for assembly of transcriptional units containing N-terminal fusions.
354 An internal BpiI site within the promoter sequence was removed during cloning by
355 introducing a nucleotide substitution via the PCR primers. For N-terminal GFP fusion
356 constructs, modules pAGM11335 (pUbi10), pICSL30006 (N-terminal GFP tag, (Engler et al.
357 2014) pNAU7 (*AtDGL1*), and pAGM16841 (tNOS, (Gantner et al. 2018) were assembled in a
358 single BsaI Golden Gate reaction into pICH47742 (Weber et al. 2011), yielding
359 pUbi10::GFP-AtDGL1::tNOS.
360 For C-terminal GFP fusion constructs, modules pAGM11323 (pUbi10), pICSL50004 (C-
361 terminal GFP tag, (Engler et al. 2014) pNAU7 (*AtDGL1*), and pICH41421 (tNOS,) (Engler et
362 al. 2014) were assembled in a single BsaI Golden Gate reaction into pICH47742, yielding
363 pUbi10::AtDGL1-GFP::tNOS.
364 All other constructs were cloned via Gateway Technology.
365
366 **Plant Growth and Chemical Treatments**
367 Seeds were surface-sterilized and germinated on 1% (w/v) Phyto-Agar (Duchefa) containing
368 2.5 mM KH_2PO_4, pH 5.6 (high Pi or +Pi medium) or no Pi supplement (low Pi or –Pi
369 medium) as reported (Naumann et al. 2022). Agar media deficient in other nutrients (C, N, or
370 Fe) or supplemented with ER stress-agents were prepared as described (Naumann et al. 2022;
371 Naumann et al. 2019). The agar was routinely purified by repeated washing in deionized
372 water and subsequent dialysis using DOWEX G-55 anion exchanger (Ticconi et al. 2009).
373 For carbon starvation experiments on soil, 6 weeks-old plants grown under short-day
374 photoperiod were transferred to darkness for 6 days followed by 7 days of recovery in short-
375 day condition (Naumann et al. 2019; Qi et al. 2023; Thompson et al. 2005). Nutrient
376 limitation in aseptic conditions was performed as follows: For carbon starvation, seedlings
377 were transferred to carbon (sucrose) deficient media 5 days after germination and kept in the

378 dark for 12 days followed by 7 days of recovery on +Pi media. For nitrogen starvation, 5
379 days-old seedlings (after germination on +Pi) were transferred to nitrogen deficient media for
380 7 days.

381 **Chemical Treatments**

382 Tunicamycin (TM) and torin treatment were performed by transferring 5-day-old seedlings
383 (germinated on +Pi) to liquid media supplemented with 5 µg/mL TM, 1 µM torin or DMSO
384 (solvent) for 5-7 h. Concanamycin A (ConA) treatment was added to a final concentration of
385 1µM for the indicated time points (3-5 h).

386 **Histochemical staining**

387 GUS (β-glucuronidase) staining was conducted as described (Naumann et al. 2022).
388 Seedlings were incubated in GUS-staining solution (50 mM Na-phosphate, pH7.2; 0.5 mM
389 $K_3Fe(CN)_6$; 0.5 mM $K_4Fe(CN)_6$; 2mM X-Gluc; 10mM EDTA; 0,1% TritonX) at 37°C and
390 subsequently cleared using chloral hydrate solution (8:2:1 chloral hydrate:glycerol: ddH_2O).
391 Iron detection, based on Perls staining coupled to diaminobenzidine (DAB) intensification
392 (Perls/DAB staining) was performed as previously described (Muller et al. 2015) with minor
393 changes to the protocol. Plants were incubated for 10 min in 2% (v/v) HCl, 4% (w/v) K-
394 ferrocyanide (Perls staining), or K-ferricyanide (Turnbull staining). For DAB intensification,
395 plants were washed twice (ddH_2O) and incubated (15 min) in methanol containing 10 mM
396 Na-azide and 0.3% (v/v) H_2O_2. After washing with 100 mM Na-phosphate buffer (pH 7.4),
397 plants were incubated for 3 min in the same buffer containing 0.025% (w/v) DAB (Sigma-
398 Aldrich) and 0.005% (v/v) H_2O_2. The reaction was stopped by washing with 100 mM Na-
399 phosphate buffer (pH 7.4) and optically clearing with chloral hydrate, 1 g/ml 15% (v/v)
400 glycerol.

401 **Confocal Microscopy**

402 Samples were analyzed using a multizoom stereomicroscope (Nikon AZ100) for overview
403 images and a Zeiss AxioImager bright field microscope for detail images. Confocal

404 microscopy was done on a Zeiss LSM900. Imaging was performed with a ×20 air, ×40 water
405 or x63 water immersion objective using sequential acquisition. For each experiment, 7-10
406 individual samples were observed in three independent approaches. Images were processed
407 using ImageJ (Schindelin et al. 2012) software. Total puncta numbers were counted using the
408 MTB Cell Counter (Franke et al. 2015). Colocalization and Pearsons coefficient were
409 calculated using the BIOP FiJi Plugin.
410 Callose was stained for 1 h with 0.1% (w/v) aniline blue (AppliChem) in 100 mM Na-
411 phosphate buffer (pH 7.2) and carefully washed twice. Fluorescence was visualized using a
412 Zeiss LSM 900 confocal laser-scanning microscope (excitation 405 nm, emission 498 nm) in
413 100 mM Na-phosphate buffer (pH 7.2) (Muller et al. 2015).
414 **Autophagosome size determination**
415 Five-day old seedlings expressing *35S::GFP-ATG8A* in WT or *cane1-c1* were transferred to
416 +Pi or -Pi for one day followed by liquid treatments to induce ER-stress by TM (5 µg/ml) or
417 torin (1 µM) treatments for 6 h. Primary root transition zones were imaged and Arivis Vision
418 4D 3.6.2 (arivis AG) was used for analysis. A custom pipeline to measure autophagosome
419 volume was set up using the Blob Finder with the following parameters: average size 2 µm,
420 probability threshold 55%, split sensitivity 50%. Sphericity was set to > 0.65 and a segment
421 feature filter was applied to ≥ 0.6 μm^2.
422 **Transient expression in *N. benthamiana***
423 Leaves of 6-week-old tobacco (*Nicotiana benthamiana*) plants were co-infiltrated with *A.*
424 *tumefaciens* harboring the respective plasmid. After 3 d, leaf discs were analyzed by confocal
425 laser scanning microscopy (GFP: excitation 488 nm, emission 493-537 nm; mCherry:
426 excitation 555 nm, emission 582-631 nm; chlorophyll autofluorescence: excitation 633 nm,
427 emission, 669-722 nm).
428 **Yeast-two-hybrid assay**
429 To perform direct Y2H test, the full length CANE1 as well as $CANE1^{F183A, V186A,}$

430 CANE1$^{W202A, V205A}$ and CANE1$^{F183A, V186A, W202A, V205A}$ (CANE1$^{\Delta AIM4}$, CANE1$^{\Delta AIM5}$ and
431 CANE1$^{\Delta AIM4,5}$ respectively), were cloned into the pDEST32 (Invitrogen) vector using
432 gateway technology, to create protein fusions with the Gal4 DNA binding domain. All nine
433 Arabidopsis ATG8 isoforms were cloned into the prey pDEST22 vector to obtain Gal4
434 activation fusions.
435 The bait and prey vectors to be tested for interaction of the fusion proteins were co-
436 transformed into *S. cerevisiae* strain PJ69-4a using the standard LiOAc method (Gietz and
437 Schiestl 2007). The yeast was spotted on plates with vector selective media DDO (double
438 drop out media: SD/-Leu/-Trp) and were grown for 4-5 days at 30°C. Two independent
439 colonies of each transformation were inoculated in 1x TE buffer and incubated at 30°C at 180
440 rpm overnight. On the next day, 10 µL of the colonies were spotted on DDO, interaction
441 selective media (triple drop out media: SD/-Leu/-Trp/-His) and triple drop out media
442 containing 2 mM 3-aminotriazole (triple drop out media: SD/-Leu/-Trp/-His/+3-
443 aminotriazole). Pictures were taken 6 days after spotting. SD plates were prepared with 1.6%
444 (w/v) Bactoagar (AppliChem) and the SD media was obtained from TakaraBio.
445 **Affinity-based Immunoprecipitation**
446 Proteins were extracted from plant material with RIPA-buffer (50 mM Tris-Cl, pH 7.6, 150
447 mM NaCl, 20 mM NaF, 10 mM $Na_4P_2O_7$, 1 mM EDTA, 0.5 mM EGTA, 1% Nonidet-P-40,
448 0.5% Na-deoxycholate, 1 mM PMSF, 1 mM DTT) for 30 min at 4°C. Post centrifugation the
449 cleared lysate was diluted 1:1 with detergent-free RIPA and incubated with equilibrated GFP-
450 trap or RFP-trap Agarose beads (ChromoTek) for 2h at 8°C on a multi-rotator. After
451 centrifugation (2500xg, 4°C) and washing 3-times (detergent-free RIPA), proteins were eluted
452 at 68°C for 15 min in 2x SDS sample buffer. The supernatant was transferred to a new tube
453 and boiled at 95°C for 5min.
454 **Immunoblotting**

455 Seedlings were germinated on +Pi medium for 5 d prior to transfer to Pi-sufficient (+Pi) or
456 deficient (-Pi) media. Whole roots were harvested 1dpt after treatments. For basal protein
457 quantification whole seedlings were directly harvested 5dpg. Proteins were extracted using
458 RIPA-buffer (50 mM Tris-Cl, pH 7.6, 150 mM NaCl, 20 mM NaF, 10 mM $Na_4P_2O_7$, 1 mM
459 EDTA, 0.5 mM EGTA, 1% Nonidet-P-40, 0.5% Na-deoxycholate, 1 mM PMSF, 1 mM DTT)
460 for 30 min at 4°C. Protein concentrations were measured using the Pierce™ 660 nm Protein-
461 Assay-Kit (Thermo Fisher, 22662). Equal amounts of total proteins were loaded on 10%
462 SDS-gels containing TCE (2,2,2-Trichlorethanol, Sigma-Aldrich, T54801) as loading control
463 (Ladner et al. 2004). All gels were simultaneously immunoblotted. All antibodies used in this
464 study are listed in Supplementary table 3.

465 **Quantitative proteomics**

466 Primary root tips were excised 24 h after transfer to the indicated media and collected into
467 liquid nitrogen. Tissue lysis, sample preparation, protein labeling, Tandem-Mass-Tag (TMT)
468 spectrometry, MS/MS data analysis, and TMT-quantifications were performed as recently
469 described (Naumann et al. 2022; Rodriguez et al. 2020; Stephani et al. 2020).
470 NanoLC-MS/MS Analysis: The nano HPLC system (Vanquish *Neo* UHPLC-System, Thermo
471 Scientific) was coupled to an Orbitrap Astral mass spectrometer, equipped with a Nanospray
472 Flex ion source (all parts Thermo Scientific). Peptides were loaded onto a trap column
473 (PepMap Acclaim C18, 5 mm × 300 µm ID, 5 µm particle size, 100 Å pore size, Thermo
474 Scientific) at a flow rate of 25 µl/min using 0.1% TFA as mobile phase.
475 After 5 minutes, the trap column was switched in line with the analytical column (Aurora
476 Ultimate C18 25cm × 75 µm ID, 1.7 µm particles, 120 Å, with integrated emitter, Ionopticks
477 operated at 50°C). Peptides were eluted using a flow rate of 300 nl/min, starting with the
478 mobile phases 98% A (0.1% formic acid in water) and 2% B (80% acetonitrile, 0.1% formic
479 acid) and linearly increasing to 35% B over the next 60 minutes, followed by an increase to

480 95% B in 1.7 min, a 4-min hold at 95% B, and re-equilibration with 2% B for three column
481 volumes (equilibration factor of 3.0).
482 The Orbitrap Astral was operated in data-dependent mode, performing a full scan in the
483 Orbitrap every 0.7 s (m/z range 375–1500 m/z; resolution 240,000; standard AGC target,
484 maximum injection time 10 ms, minimum intensity 5,000). MS/MS spectra were acquired in
485 the Astral analyser by isolating 1.6 Da windows and fragmenting precursor ions with
486 normalized HCD collision energy of 30% with a maximum injection time of 5 or 10 ms
487 correspondingly or until a standard AGC target was reached. Fragment ions ranging from
488 150–2000 m/z were acquired. Precursor ions selected for fragmentation (include charge state
489 2-6) were put on a dynamic exclusion list for 30 s.

490 **qRT PCR**

491 Abundance of mRNAs was quantified using fluorescence-based real-time RT-PCR and gene-
492 specific amplimers listed in Supplementary table 1. Relative mRNA abundances were
493 normalized relative to *UBC9* transcript abundance. Samples from three independent
494 experiments were measured.

495 **Phylogenetic Analysis**

496 CANE1 sequence alignment and phylogenetic analysis were done using BLAST search of
497 curated sequences in the NCBI database and phytozome 13. Obtained sequences were filtered
498 for fragments. All phylogenetic trees were calculated by sequence alignment using MAFFT
499 7108 with default settings and created at the CIPRES web-portal with RAxML 8.2.10109 for
500 maximum likelihood analyses using the JTT PAM matrix for amino acid substitutions in
501 RAxML. All related sequences used for phylogenetic analyses are provided (Supplementary
502 Data 2).

503 **Quantification and Statistical Analysis**

504 All claims of statistical significance can be found in the corresponding figure legends.
505 Statistical tests were carried out using GraphPad Prism 10 for Windows.

506 **Acknowledgements** We thank P.J. Hussey and P. Wang for seeds; M. Ried and S. Abel for
507 scientific discussions and critical reading of the manuscript. This work was supported by the
508 Deutsche Forschungsgemeinschaft (DFG, German Research Foundation) projects 492493685
509 and 400681449/GRK 2498.; an EMBO Short-Term Fellowship to C.N. and institutional core
510 funding (Leibniz Association) from the Federal Republic of Germany and the State of
511 Saxony-Anhalt. Work in the K.M. group was financially supported by the EPIC-XS (project
512 number 823839), the Horizon 2020 Program of the European Union, and the ERA-CAPS I
513 3686 project of the Austrian Science Fund.

514 **Author contributions** D.G. and C.N. designed research; D.G., F.S., K.M., J.A., F.K., S.M.,
515 Y.TN., N.G. and S.H. conducted experiments and analyzed data; K.M. and R.I. performed
516 proteomic analysis; Y.D. and C.N. supervised the project; D.G. drafted the manuscript; C.N.
517 wrote the article.

518 **Competing interests** The authors declare no competing interests.

519 **LITERATURE CITED**

520 Abel S (2017) Phosphate scouting by root tips. Curr Opin Plant Biol 39:168-177.
521 doi:10.1016/j.pbi.2017.04.016
522 Abel S, Naumann C (2024) Evolution of phosphate scouting in the terrestrial biosphere.
523 Philos Trans R Soc Lond B Biol Sci 379 (1914):20230355.
524 doi:10.1098/rstb.2023.0355
525 Balzergue C, Dartevelle T, Godon C, Laugier E, Meisrimler C, Teulon JM, Creff A, Bissler
526 M, Brouchoud C, Hagege A, Muller J, Chiarenza S, Javot H, Becuwe-Linka N, David
527 P, Peret B, Delannoy E, Thibaud MC, Armengaud J, Abel S, Pellequer JL, Nussaume
528 L, Desnos T (2017) Low phosphate activates STOP1-ALMT1 to rapidly inhibit root
529 cell elongation. Nat Commun 8:15300. doi:10.1038/ncomms15300
530 Cadena-Ramos AI, De-la-Pena C (2024) Picky eaters: selective autophagy in plant cells. Plant
531 J 117 (2):364-384. doi:10.1111/tpj.16508
532 Clua J, Montpetit J, Jimenez-Sandoval P, Naumann C, Santiago J, Poirier Y (2024) A
533 CYBDOM protein impacts iron homeostasis and primary root growth under phosphate
534 deficiency in Arabidopsis. Nat Commun 15 (1):423. doi:10.1038/s41467-023-43911-x
535 Crombez H, Motte H, Beeckman T (2019) Tackling Plant Phosphate Starvation by the Roots.
536 Dev Cell 48 (5):599-615. doi:10.1016/j.devcel.2019.01.002
537 Del Chiaro A, Grujic N, Zhao J, Papareddy RK, Gao P, Ma J, Lofke C, Bhattacharya A,
538 Gruetzner R, Bourguet P, Berger F, Kang BH, Marillonnet S, Dagdas Y (2025)
539 Nonuple atg8 mutant provides genetic evidence for functional specialization of ATG8
540 isoforms in Arabidopsis thaliana. J Cell Sci. doi:10.1242/jcs.263803
541 Dong K, Deng G, Liu Y, Chen KE, Wei H, Huang X, Huang W, Zheng P, Ueda T, Vierstra
542 RD, Huang X, Li F (2025) Comprehensive genetic analyses of Arabidopsis
543 autophagy-related 8 family reveal redundant regulatory roles during autophagy. New
544 Phytol. doi:10.1111/nph.70418
545 Engler C, Youles M, Gruetzner R, Ehnert TM, Werner S, Jones JD, Patron NJ, Marillonnet S
546 (2014) A golden gate modular cloning toolbox for plants. ACS Synth Biol 3 (11):839-
547 843. doi:10.1021/sb4001504
548 Feng Q, De Rycke R, Dagdas Y, Nowack MK (2022) Autophagy promotes programmed cell
549 death and corpse clearance in specific cell types of the Arabidopsis root cap. Curr Biol
550 32 (20):4548. doi:10.1016/j.cub.2022.10.006
551 Feng Z, Zhao Y, Li T, Nie W, Yang X, Wang X, Wu J, Liao J, Zou Y (2020) CATP-8/P5A
552 ATPase Regulates ER Processing of the DMA-1 Receptor for Dendritic Branching.
553 Cell Rep 32 (10):108101. doi:10.1016/j.celrep.2020.108101
554 Gantner J, Ordon J, Ilse T, Kretschmer C, Gruetzner R, Lofke C, Dagdas Y, Burstenbinder K,
555 Marillonnet S, Stuttmann J (2018) Peripheral infrastructure vectors and an extended
556 set of plant parts for the Modular Cloning system. PLoS One 13 (5):e0197185.
557 doi:10.1371/journal.pone.0197185
558 Giehl RF, von Wiren N (2014) Root nutrient foraging. Plant Physiol 166 (2):509-517.
559 doi:10.1104/pp.114.245225
560 Gietz RD, Schiestl RH (2007) High-efficiency yeast transformation using the LiAc/SS carrier
561 DNA/PEG method. Nat Protoc 2 (1):31-34. doi:10.1038/nprot.2007.13
562 Gong F, Yao Z, Liu Y, Sun M, Peng X (2021) H(2)O(2) response gene 1/2 are novel sensors
563 or responders of H(2)O(2) and involve in maintaining embryonic root meristem
564 activity in Arabidopsis thaliana. Plant Sci 310:110981.
565 doi:10.1016/j.plantsci.2021.110981
566 Gross AS, Raffeiner M, Zeng Y, Ustun S, Dagdas Y (2025) Autophagy in Plant Health and
567 Disease. Annu Rev Plant Biol 76 (1):197-227. doi:10.1146/annurev-arplant-060324-
568 094912

569 Gutierrez-Alanis D, Yong-Villalobos L, Jimenez-Sandoval P, Alatorre-Cobos F, Oropeza-
570 Aburto A, Mora-Macias J, Sanchez-Rodriguez F, Cruz-Ramirez A, Herrera-Estrella L
571 (2017) Phosphate Starvation-Dependent Iron Mobilization Induces CLE14 Expression
572 to Trigger Root Meristem Differentiation through CLV2/PEPR2 Signaling. Dev Cell
573 41 (5):555-570 e553. doi:10.1016/j.devcel.2017.05.009
574 Jakobsen MK, Poulsen LR, Schulz A, Fleurat-Lessard P, Moller A, Husted S, Schiott M,
575 Amtmann A, Palmgren MG (2005) Pollen development and fertilization in
576 Arabidopsis is dependent on the MALE GAMETOGENESIS IMPAIRED ANTHERS
577 gene encoding a type V P-type ATPase. Genes Dev 19 (22):2757-2769.
578 doi:10.1101/gad.357305
579 Ji J, Cui MK, Zou R, Wu MZ, Ge MX, Li J, Zhang ZR (2024) An ATP13A1-assisted
580 topogenesis pathway for folding multi-spanning membrane proteins. Mol Cell 84
581 (10):1917-1931 e1915. doi:10.1016/j.molcel.2024.04.010
582 Johansen T, Lamark T (2020) Selective Autophagy: ATG8 Family Proteins, LIR Motifs and
583 Cargo Receptors. J Mol Biol 432 (1):80-103. doi:10.1016/j.jmb.2019.07.016
584 Jung H, Lee HN, Marshall RS, Lomax AW, Yoon MJ, Kim J, Kim JH, Vierstra RD, Chung T
585 (2020) Arabidopsis cargo receptor NBR1 mediates selective autophagy of defective
586 proteins. J Exp Bot 71 (1):73-89. doi:10.1093/jxb/erz404
587 Kellermeier F, Armengaud P, Seditas TJ, Danku J, Salt DE, Amtmann A (2014) Analysis of
588 the Root System Architecture of Arabidopsis Provides a Quantitative Readout of
589 Crosstalk between Nutritional Signals. Plant Cell 26 (4):1480-1496.
590 doi:10.1105/tpc.113.122101
591 L. Franke BS, J. L. Erickson, D. Rödel, D. Schröter, B. Möller, and M. H. Schattat (2015) The
592 'MTB Cell Counter' a versatile tool for the semi-automated quantification of sub-
593 cellular phenotypes in fluorescence microscopy images. A case study on plastids,
594 nuclei and peroxisomes. Journal of Endocytobiosis and Cell Research 26:31-42
595 Labun K, Montague TG, Krause M, Torres Cleuren YN, Tjeldnes H, Valen E (2019)
596 CHOPCHOP v3: expanding the CRISPR web toolbox beyond genome editing.
597 Nucleic Acids Res 47 (W1):W171-W174. doi:10.1093/nar/gkz365
598 Ladner CL, Yang J, Turner RJ, Edwards RA (2004) Visible fluorescent detection of proteins
599 in polyacrylamide gels without staining. Anal Biochem 326 (1):13-20.
600 doi:10.1016/j.ab.2003.10.047
601 Lai Z, Wang F, Zheng Z, Fan B, Chen Z (2011) A critical role of autophagy in plant
602 resistance to necrotrophic fungal pathogens. Plant J 66 (6):953-968.
603 doi:10.1111/j.1365-313X.2011.04553.x
604 Lambers H, Martinoia E, Renton M (2015) Plant adaptations to severely phosphorus-
605 impoverished soils. Curr Opin Plant Biol 25:23-31. doi:10.1016/j.pbi.2015.04.002
606 Lerouxel O, Mouille G, Andeme-Onzighi C, Bruyant MP, Seveno M, Loutelier-Bourhis C,
607 Driouich A, Hofte H, Lerouge P (2005) Mutants in DEFECTIVE
608 GLYCOSYLATION, an Arabidopsis homolog of an oligosaccharyltransferase
609 complex subunit, show protein underglycosylation and defects in cell differentiation
610 and growth. Plant J 42 (4):455-468. doi:10.1111/j.1365-313X.2005.02392.x
611 Li C, Duckney P, Zhang T, Fu Y, Li X, Kroon J, De Jaeger G, Cheng Y, Hussey PJ, Wang P
612 (2022) TraB family proteins are components of ER-mitochondrial contact sites and
613 regulate ER-mitochondrial interactions and mitophagy. Nat Commun 13 (1):5658.
614 doi:10.1038/s41467-022-33402-w
615 Li P, Bagenholm V, Hagglund P, Lindkvist-Petersson K, Wang K, Gourdon P (2024) The
616 structure and function of P5A-ATPases. Nat Commun 15 (1):9605.
617 doi:10.1038/s41467-024-53757-6

618 Li T, Yang X, Feng Z, Nie W, Fang Z, Zou Y (2021) P5A ATPase controls ER translocation
619 of Wnt in neuronal migration. Cell Rep 37 (4):109901.
620 doi:10.1016/j.celrep.2021.109901
621 Limpens E, Ramos J, Franken C, Raz V, Compaan B, Franssen H, Bisseling T, Geurts R
622 (2004) RNA interference in Agrobacterium rhizogenes-transformed roots of
623 Arabidopsis and Medicago truncatula. J Exp Bot 55 (399):983-992.
624 doi:10.1093/jxb/erh122
625 Liu F, Hu W, Li F, Marshall RS, Zarza X, Munnik T, Vierstra RD (2020) AUTOPHAGY-
626 RELATED14 and Its Associated Phosphatidylinositol 3-Kinase Complex Promote
627 Autophagy in Arabidopsis. Plant Cell 32 (12):3939-3960. doi:10.1105/tpc.20.00285
628 Liu W, Liu Z, Mo Z, Guo S, Liu Y, Xie Q (2021) ATG8-Interacting Motif: Evolution and
629 Function in Selective Autophagy of Targeting Biological Processes. Front Plant Sci
630 12:783881. doi:10.3389/fpls.2021.783881
631 Liu Y, Bassham DC (2012) Autophagy: pathways for self-eating in plant cells. Annu Rev
632 Plant Biol 63:215-237. doi:10.1146/annurev-arplant-042811-105441
633 Man Y, Zhang Y, Chen L, Zhou J, Bu Y, Zhang X, Li X, Li Y, Jing Y, Lin J (2024) The
634 VAMP-associated protein VAP27-1 plays a crucial role in plant resistance to ER
635 stress by modulating ER-PM contact architecture in Arabidopsis. Plant Commun 5
636 (7):100929. doi:10.1016/j.xplc.2024.100929
637 Maniero RA, Picco C, Hartmann A, Engelberger F, Gradogna A, Scholz-Starke J, Melzer M,
638 Kunze G, Carpaneto A, von Wiren N, Giehl RFH (2024) Ferric reduction by a
639 CYBDOM protein counteracts increased iron availability in root meristems induced
640 by phosphorus deficiency. Nat Commun 15 (1):422. doi:10.1038/s41467-023-43912-
641 w
642 McKenna MJ, Adams BM, Chu V, Paulo JA, Shao S (2022) ATP13A1 prevents ERAD of
643 folding-competent mislocalized and misoriented proteins. Mol Cell 82 (22):4277-4289
644 e4210. doi:10.1016/j.molcel.2022.09.035
645 McKenna MJ, Sim SI, Ordureau A, Wei L, Harper JW, Shao S, Park E (2020) The
646 endoplasmic reticulum P5A-ATPase is a transmembrane helix dislocase. Science 369
647 (6511). doi:10.1126/science.abc5809
648 Muller J, Toev T, Heisters M, Teller J, Moore KL, Hause G, Dinesh DC, Burstenbinder K,
649 Abel S (2015) Iron-dependent callose deposition adjusts root meristem maintenance to
650 phosphate availability. Dev Cell 33 (2):216-230. doi:10.1016/j.devcel.2015.02.007
651 Nakatogawa H (2020) Mechanisms governing autophagosome biogenesis. Nat Rev Mol Cell
652 Biol 21 (8):439-458. doi:10.1038/s41580-020-0241-0
653 Nascimbeni AC, Codogno P, Morel E (2017) Phosphatidylinositol-3-phosphate in the
654 regulation of autophagy membrane dynamics. FEBS J 284 (9):1267-1278.
655 doi:10.1111/febs.13987
656 Naumann C, Heisters M, Brandt W, Janitza P, Alfs C, Tang N, Toto Nienguesso A, Ziegler J,
657 Imre R, Mechtler K, Dagdas Y, Hoehenwarter W, Sawers G, Quint M, Abel S (2022)
658 Bacterial-type ferroxidase tunes iron-dependent phosphate sensing during Arabidopsis
659 root development. Curr Biol 32 (10):2189-2205 e2186. doi:10.1016/j.cub.2022.04.005
660 Naumann C, Muller J, Sakhonwasee S, Wieghaus A, Hause G, Heisters M, Burstenbinder K,
661 Abel S (2019) The Local Phosphate Deficiency Response Activates Endoplasmic
662 Reticulum Stress-Dependent Autophagy. Plant Physiol 179 (2):460-476.
663 doi:10.1104/pp.18.01379
664 Nthiga TM, Kumar Shrestha B, Sjottem E, Bruun JA, Bowitz Larsen K, Bhujabal Z, Lamark
665 T, Johansen T (2020) CALCOCO1 acts with VAMP-associated proteins to mediate
666 ER-phagy. EMBO J 39 (15):e103649. doi:10.15252/embj.2019103649

667 Ordon J, Gantner J, Kemna J, Schwalgun L, Reschke M, Streubel J, Boch J, Stuttmann J
668 (2017) Generation of chromosomal deletions in dicotyledonous plants employing a
669 user-friendly genome editing toolkit. Plant J 89 (1):155-168. doi:10.1111/tpj.13319
670 Petersen M, Avin-Wittenberg T, Bassham DC, Dagdas Y, Fan C, Fernie AR, Jiang L, Mishra
671 D, Otegui MS, Rodriguez E, Hofius D (2024) Autophagy in plants. Autophagy Rep 3
672 (1):2395731. doi:10.1080/27694127.2024.2395731
673 Picchianti L, Sanchez de Medina Hernandez V, Zhan N, Irwin NA, Groh R, Stephani M,
674 Hornegger H, Beveridge R, Sawa-Makarska J, Lendl T, Grujic N, Naumann C,
675 Martens S, Richards TA, Clausen T, Ramundo S, Karagoz GE, Dagdas Y (2023)
676 Shuffled ATG8 interacting motifs form an ancestral bridge between UFMylation and
677 autophagy. EMBO J 42 (10):e112053. doi:10.15252/embj.2022112053
678 Qi H, Wang Y, Bao Y, Bassham DC, Chen L, Chen QF, Hou S, Hwang I, Huang L, Lai Z, Li
679 F, Liu Y, Qiu R, Wang H, Wang P, Xie Q, Zeng Y, Zhuang X, Gao C, Jiang L, Xiao S
680 (2023) Studying plant autophagy: challenges and recommended methodologies. Adv
681 Biotechnol (Singap) 1 (4):2. doi:10.1007/s44307-023-00002-8
682 Qin Q, Zhao T, Zou W, Shen K, Wang X (2020) An Endoplasmic Reticulum ATPase
683 Safeguards Endoplasmic Reticulum Identity by Removing Ectopically Localized
684 Mitochondrial Proteins. Cell Rep 33 (6):108363. doi:10.1016/j.celrep.2020.108363
685 Rodriguez E, Chevalier J, Olsen J, Ansbol J, Kapousidou V, Zuo Z, Svenning S, Loefke C,
686 Koemeda S, Drozdowskyj PS, Jez J, Durnberger G, Kuenzl F, Schutzbier M, Mechtler
687 K, Ebstrup EN, Lolle S, Dagdas Y, Petersen M (2020) Autophagy mediates temporary
688 reprogramming and dedifferentiation in plant somatic cells. EMBO J 39 (4):e103315.
689 doi:10.15252/embj.2019103315
690 Rogov VV, Nezis IP, Tsapras P, Zhang H, Dagdas Y, Noda NN, Nakatogawa H, Wirth M,
691 Mouilleron S, McEwan DG, Behrends C, Deretic V, Elazar Z, Tooze SA, Dikic I,
692 Lamark T, Johansen T (2023) Atg8 family proteins, LIR/AIM motifs and other
693 interaction modes. Autophagy Rep 2 (1). doi:10.1080/27694127.2023.2188523
694 Schindelin J, Arganda-Carreras I, Frise E, Kaynig V, Longair M, Pietzsch T, Preibisch S,
695 Rueden C, Saalfeld S, Schmid B, Tinevez JY, White DJ, Hartenstein V, Eliceiri K,
696 Tomancak P, Cardona A (2012) Fiji: an open-source platform for biological-image
697 analysis. Nat Methods 9 (7):676-682. doi:10.1038/nmeth.2019
698 Shen J, Yuan L, Zhang J, Li H, Bai Z, Chen X, Zhang W, Zhang F (2011) Phosphorus
699 dynamics: from soil to plant. Plant Physiol 156 (3):997-1005.
700 doi:10.1104/pp.111.175232
701 Shin KD, Lee HN, Chung T (2014) A revised assay for monitoring autophagic flux in
702 Arabidopsis thaliana reveals involvement of AUTOPHAGY-RELATED9 in
703 autophagy. Mol Cells 37 (5):399-405. doi:10.14348/molcells.2014.0042
704 Sim SI, Park E (2023) P5-ATPases: Structure, substrate specificities, and transport
705 mechanisms. Curr Opin Struct Biol 79:102531. doi:10.1016/j.sbi.2023.102531
706 Stefano G, Renna L, Wormsbaecher C, Gamble J, Zienkiewicz K, Brandizzi F (2018) Plant
707 Endocytosis Requires the ER Membrane-Anchored Proteins VAP27-1 and VAP27-3.
708 Cell Rep 23 (8):2299-2307. doi:10.1016/j.celrep.2018.04.091
709 Stephani M, Dagdas Y (2020) Plant Selective Autophagy-Still an Uncharted Territory With a
710 Lot of Hidden Gems. J Mol Biol 432 (1):63-79. doi:10.1016/j.jmb.2019.06.028
711 Stephani M, Picchianti L, Dagdas Y (2021) C53 is a cross-kingdom conserved reticulophagy
712 receptor that bridges the gap betweenselective autophagy and ribosome stalling at the
713 endoplasmic reticulum. Autophagy 17 (2):586-587.
714 doi:10.1080/15548627.2020.1846304
715 Stephani M, Picchianti L, Gajic A, Beveridge R, Skarwan E, Sanchez de Medina Hernandez
716 V, Mohseni A, Clavel M, Zeng Y, Naumann C, Matuszkiewicz M, Turco E, Loefke C,
717 Li B, Durnberger G, Schutzbier M, Chen HT, Abdrakhmanov A, Savova A, Chia KS,

718 Djamei A, Schaffner I, Abel S, Jiang L, Mechtler K, Ikeda F, Martens S, Clausen T,
719 Dagdas Y (2020) A cross-kingdom conserved ER-phagy receptor maintains
720 endoplasmic reticulum homeostasis during stress. Elife 9. doi:10.7554/eLife.58396
721 Stuttmann J, Barthel K, Martin P, Ordon J, Erickson JL, Herr R, Ferik F, Kretschmer C,
722 Berner T, Keilwagen J, Marillonnet S, Bonas U (2021) Highly efficient multiplex
723 editing: one-shot generation of 8x Nicotiana benthamiana and 12x Arabidopsis
724 mutants. Plant J 106 (1):8-22. doi:10.1111/tpj.15197
725 Su T, Li X, Yang M, Shao Q, Zhao Y, Ma C, Wang P (2020) Autophagy: An Intracellular
726 Degradation Pathway Regulating Plant Survival and Stress Response. Front Plant Sci
727 11:164. doi:10.3389/fpls.2020.00164
728 Suzuki NN, Yoshimoto K, Fujioka Y, Ohsumi Y, Inagaki F (2005) The crystal structure of
729 plant ATG12 and its biological implication in autophagy. Autophagy 1 (2):119-126.
730 doi:10.4161/auto.1.2.1859
731 Svenning S, Lamark T, Krause K, Johansen T (2011) Plant NBR1 is a selective autophagy
732 substrate and a functional hybrid of the mammalian autophagic adapters NBR1 and
733 p62/SQSTM1. Autophagy 7 (9):993-1010. doi:10.4161/auto.7.9.16389
734 Svistoonoff S, Creff A, Reymond M, Sigoillot-Claude C, Ricaud L, Blanchet A, Nussaume L,
735 Desnos T (2007) Root tip contact with low-phosphate media reprograms plant root
736 architecture. Nat Genet 39 (6):792-796. doi:10.1038/ng2041
737 Thompson AR, Doelling JH, Suttangkakul A, Vierstra RD (2005) Autophagic nutrient
738 recycling in Arabidopsis directed by the ATG8 and ATG12 conjugation pathways.
739 Plant Physiol 138 (4):2097-2110. doi:10.1104/pp.105.060673
740 Ticconi CA, Delatorre CA, Abel S (2001) Attenuation of phosphate starvation responses by
741 phosphite in Arabidopsis. Plant Physiol 127 (3):963-972
742 Ticconi CA, Lucero RD, Sakhonwasee S, Adamson AW, Creff A, Nussaume L, Desnos T,
743 Abel S (2009) ER-resident proteins PDR2 and LPR1 mediate the developmental
744 response of root meristems to phosphate availability. Proc Natl Acad Sci U S A 106
745 (33):14174-14179. doi:10.1073/pnas.0901778106
746 Walczak M, Martens S (2013) Dissecting the role of the Atg12-Atg5-Atg16 complex during
747 autophagosome formation. Autophagy 9 (3):424-425. doi:10.4161/auto.22931
748 Wang P, Pleskot R, Zang J, Winkler J, Wang J, Yperman K, Zhang T, Wang K, Gong J, Guan
749 Y, Richardson C, Duckney P, Vandorpe M, Mylle E, Fiserova J, Van Damme D,
750 Hussey PJ (2019) Plant AtEH/Pan1 proteins drive autophagosome formation at ER-
751 PM contact sites with actin and endocytic machinery. Nat Commun 10 (1):5132.
752 doi:10.1038/s41467-019-12782-6
753 Wang P, Richardson C, Hawkins TJ, Sparkes I, Hawes C, Hussey PJ (2016) Plant VAP27
754 proteins: domain characterization, intracellular localization and role in plant
755 development. New Phytol 210 (4):1311-1326. doi:10.1111/nph.13857
756 Wang Y, Nishimura MT, Zhao T, Tang D (2011) ATG2, an autophagy-related protein,
757 negatively affects powdery mildew resistance and mildew-induced cell death in
758 Arabidopsis. Plant J 68 (1):74-87. doi:10.1111/j.1365-313X.2011.04669.x
759 Weber E, Engler C, Gruetzner R, Werner S, Marillonnet S (2011) A modular cloning system
760 for standardized assembly of multigene constructs. PLoS One 6 (2):e16765.
761 doi:10.1371/journal.pone.0016765
762 Wild P, McEwan DG, Dikic I (2014) The LC3 interactome at a glance. J Cell Sci 127 (Pt
763 1):3-9. doi:10.1242/jcs.140426
764 Wilfling F, Lee CW, Erdmann PS, Zheng Y, Sherpa D, Jentsch S, Pfander B, Schulman BA,
765 Baumeister W (2020) A Selective Autophagy Pathway for Phase-Separated Endocytic
766 Protein Deposits. Mol Cell 80 (5):764-778 e767. doi:10.1016/j.molcel.2020.10.030

767 Yang SY, Lin WY, Hsiao YM, Chiou TJ (2024) Milestones in understanding transport,
768 sensing, and signaling of the plant nutrient phosphorus. Plant Cell 36 (5):1504-1523.
769 doi:10.1093/plcell/koad326
770 Yoshitake Y, Nakamura S, Shinozaki D, Izumi M, Yoshimoto K, Ohta H, Shimojima M
771 (2021) RCB-mediated chlorophagy caused by oversupply of nitrogen suppresses
772 phosphate-starvation stress in plants. Plant Physiol 185 (2):318-330.
773 doi:10.1093/plphys/kiaa030
774 Yoshitake Y, Shinozaki D, Yoshimoto K (2022) Autophagy triggered by iron-mediated ER
775 stress is an important stress response to the early phase of Pi starvation in plants. Plant
776 J 110 (5):1370-1381. doi:10.1111/tpj.15743
777 Zhao D, Zou CX, Liu XM, Jiang ZD, Yu ZQ, Suo F, Du TY, Dong MQ, He W, Du LL (2020)
778 A UPR-Induced Soluble ER-Phagy Receptor Acts with VAPs to Confer ER Stress
779 Resistance. Mol Cell 79 (6):963-977 e963. doi:10.1016/j.molcel.2020.07.019
780 Zhao J, Bui MT, Ma J, Kunzl F, Picchianti L, De La Concepcion JC, Chen Y, Petsangouraki
781 S, Mohseni A, Garcia-Leon M, Gomez MS, Giannini C, Gwennogan D, Kobylinska
782 R, Clavel M, Schellmann S, Jaillais Y, Friml J, Kang BH, Dagdas Y (2022) Plant
783 autophagosomes mature into amphisomes prior to their delivery to the central vacuole.
784 J Cell Biol 221 (12). doi:10.1083/jcb.202203139
785 Zheng X, Zhao C, Liu Y (2018) Examining Autophagy in Plant by Transmission Electron
786 Microscopy (TEM). Bio Protoc 8 (20):e3047. doi:10.21769/BioProtoc.3047
787 Zhuang X, Wang H, Lam SK, Gao C, Wang X, Cai Y, Jiang L (2013) A BAR-domain protein
788 SH3P2, which binds to phosphatidylinositol 3-phosphate and ATG8, regulates
789 autophagosome formation in Arabidopsis. Plant Cell 25 (11):4596-4615.
790 doi:10.1105/tpc.113.118307

Figure 1

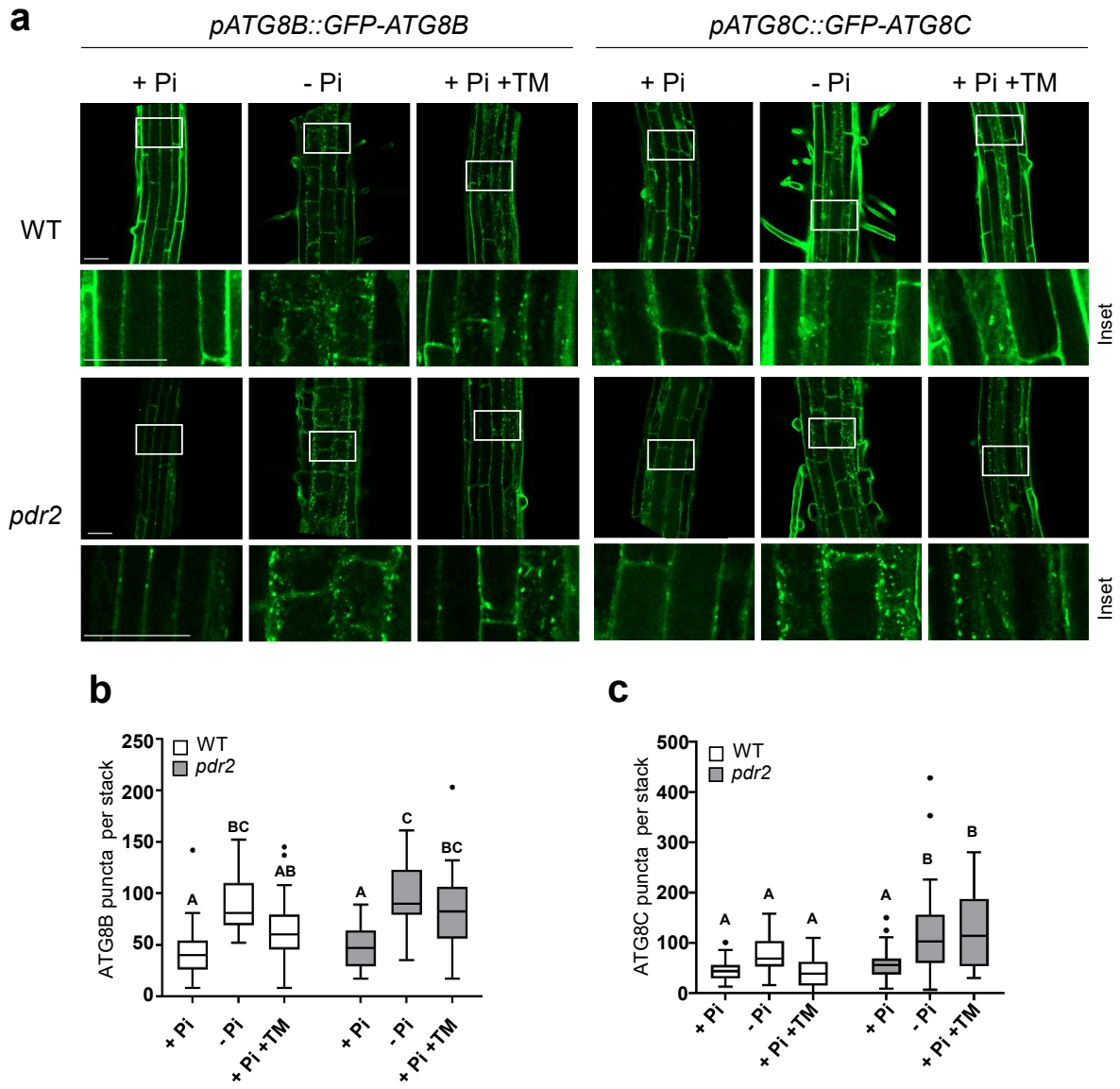

Figure 1: ER stress-induced autophagy by local Pi-sensing specifically activates ATG8B and ATG8C decorated autophagosomes. a, GFP-ATG8B and C labeled autophagosomes in Pi-deprived root tips. GFP-ATG8B/C derived fluorescence in primary root tips of transgenic (*pATG8B/C::GFP-ATG8B/C*) wildtype and *pdr2* seedlings after germination on +Pi agar (5 d) and subsequent transfer to –Pi medium for 0-24 h or treatment with 5 µg/mL tunicamycin (TM) for 6 h. Shown are representative images from three independent experiments fused Z-stacks of the transition zone. Rectangle indicate inset selection. Scale bars, 50 µm. **b** and **c**, Quantification of dataset shown in (**a**). Quantification of GFP-ATG8 puncta in root cells per normalized area. Box plots show medians and interquartile ranges of detected autophagosomes; outliers (>1.53 interquartile range) are shown as black dots. Letters denote statistical differences in condition at $p < 0.05$ (Two-way ANOVA and Tukey's HSD post hoc test) and $n \geq 27$.

Figure 2

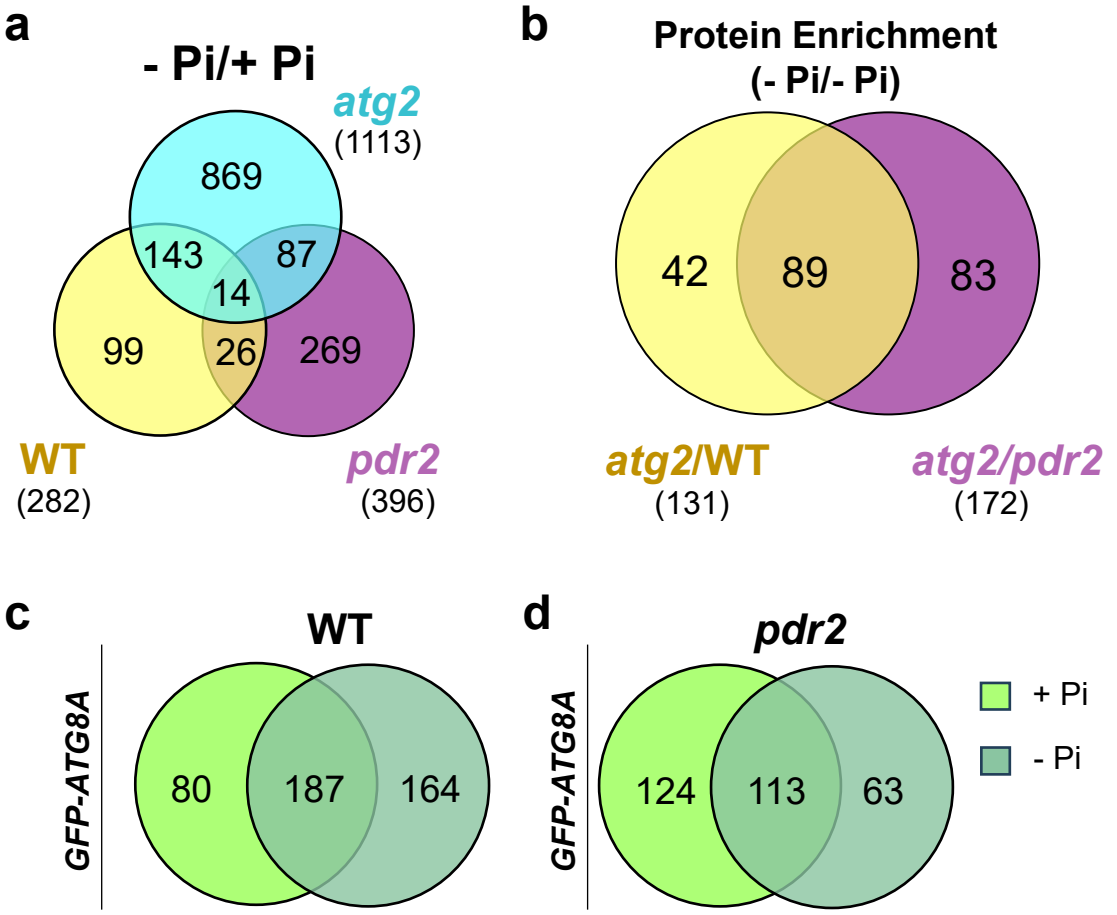

e

Fold Change		ATG8 Interaction		ID	name
WT	*pdr2*	WT	*pdr2*		
3.52	**3.67**	**yes**	**yes**	AT5G40690.1	CANE1
2.40	**2.33**	**yes**	**yes**	AT4G04620.2	ATG8B
1.91	**1.88**	**yes**	**yes**	AT1G62040.2	ATG8C
1.81	1.78	**yes**	**yes**	AT1G44770.1	unknown protein
1.72	1.76	**yes**	**yes**	AT4G24690.1	NBR1
1.33	1.35	**yes**	**yes**	AT3G49490.1	unknown protein

Figure 2: Autophagy modulates root tip proteome composition. a, Seedlings were germinated 5 days prior to transfer to the indicated treatments. 24 h post transfer primary root tips were excised and either directly subjected to extraction and quantification by mass-spectrometry (TMT-analysis) or used for co-immunoprecipitation followed by MS analysis. Venn diagram of three overlapping pairwise comparisons for root tip TMT-MS conducted in wildtype (yellow), *pdr2* (magenta) and *atg2* (cyan) plants: wildtype (-Pi) vs wildtype (+Pi) yellow cycle, *pdr2* (-Pi) vs. *pdr2* (+Pi) magenta cycle, *atg2* (-Pi) vs. *atg2* (+Pi) cyan cycle. Protein abundances with 0.6 > FC > 1.3. Total numbers are depicted in brackets. **b**, Overlap between proteins detected in –Pi conditions enriched in *atg2* compared to wildtype (yellow) or *pdr2-1* (magenta) identified by quantitative MS, FC > 1.3. Intersections show proteins with increased abundance in *atg2* but not in wildtype or *pdr2-1*. **c**,**d** *In vitro* interactome of GFP-ATG8A. Root extracts of GFP-ATG8A in transgenic wildtype (WT, **c**) and *pdr2* (**d**) primary roots were incubated with GFP-Trap beads and interacting proteins were analyzed by MS. Venn diagram of proteins co-eluting with GFP-ATG8A in +Pi (light green) and -Pi (dark green) according to the genotype. **e**, Summarized results of data obtained in c and d. Fold-Change (log2) of normalized protein abundances in *atg2* compared to wildtype (first column) and *pdr2* (second column) in -Pi conditions.

Figure 3

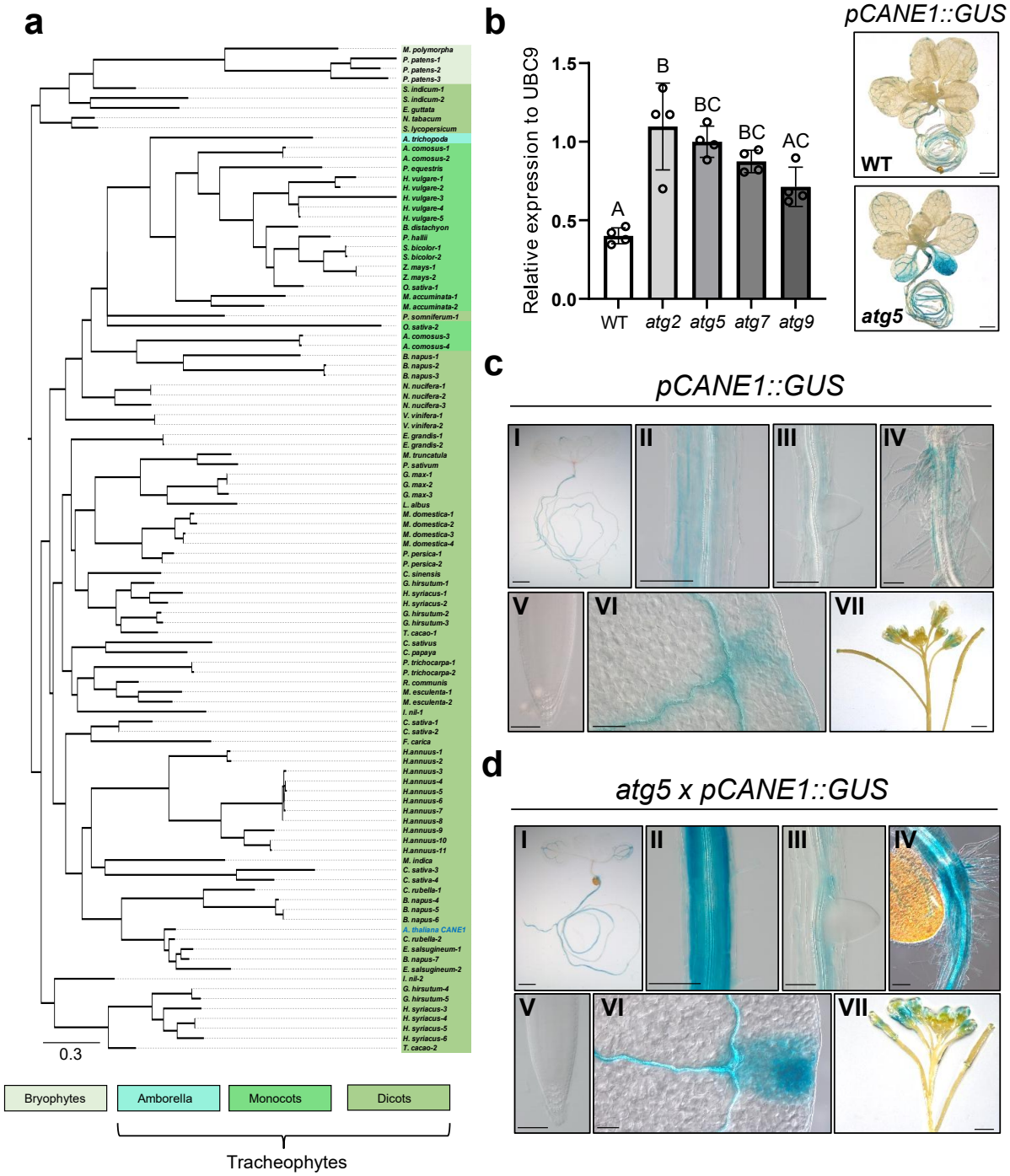

Figure 3: CANE1 is a plant specific protein. a, Maximum-likelihood midpoint-rooted tree (400 bootstrap replicates) of full-length CANE1 orthologues (see Supplementary Data 2). **b-d**, *CANE1* gene is predominantly expressed in root tissue and elevated in autophagy mutant plants. **b**, Left panel: RT-qPCR analysis of *CANE1* transcript abundance relative to *UBC9* in seedlings of wildtype, *atg2*, *atg5*, *atg7* and *atg9,* n = 4; right panel: *pCANE1::GUS* activity in 3 week old seedlings of wildtype and *atg5,* scale bar 1 cm. **c,d**, *pCANE1::GUS* activity in 7 days old wildtype (c) and *atg5* (d) seedlings (I), root elongation zone (II), lateral root emergence (III), root-shoot junction (IV), primary root tip (V), true leaf tip (VI) and flower (VII), I-VI scale bar 100 µm, VII scale bar 1 cm, n ≥ 8.

Figure 4

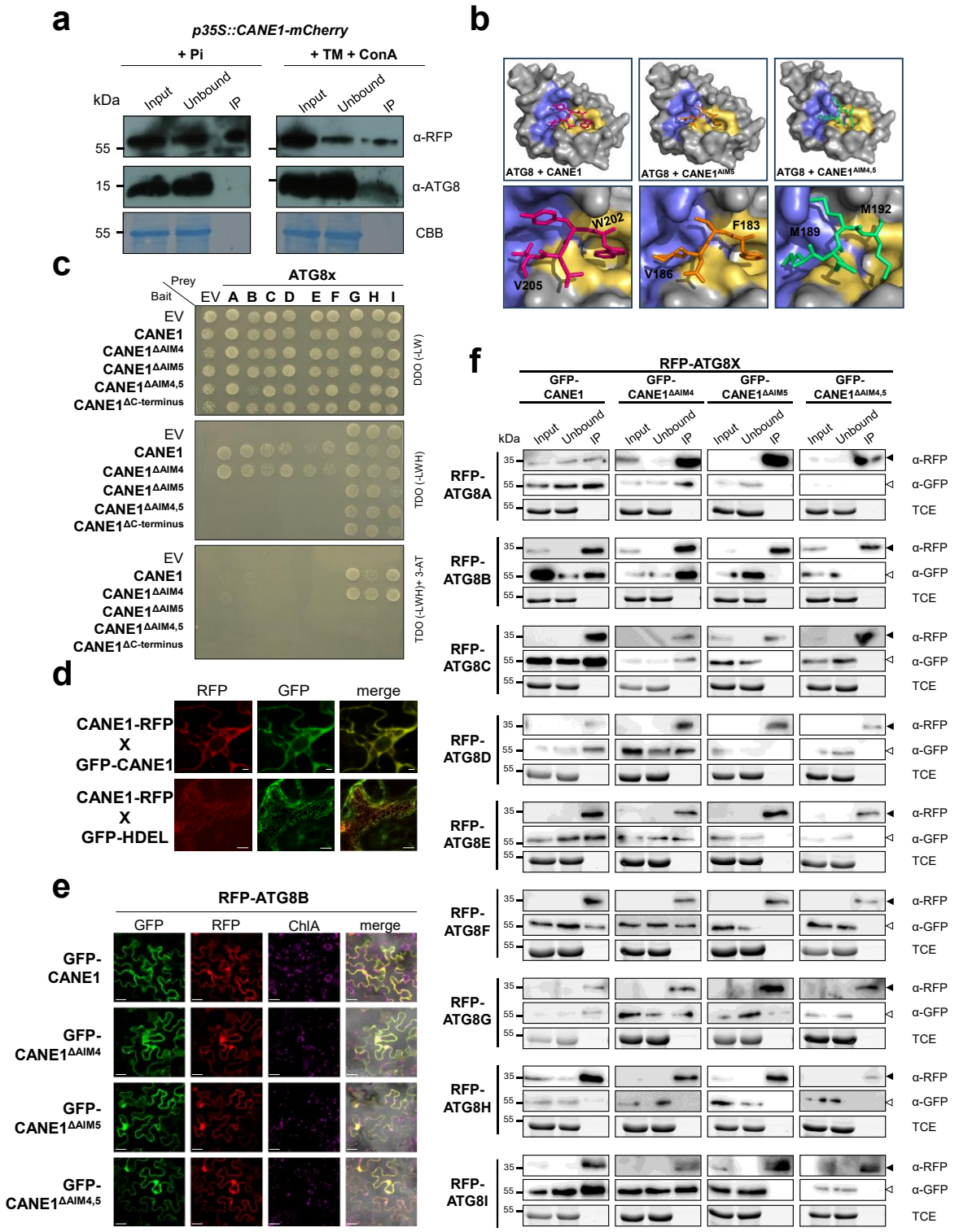
a
p35S::CANE1-mCherry
+ Pi
+ TM + ConA
kDa
Input
Unbound
IP
55
15
55
α-RFP
α-ATG8
CBB
b
ATG8 + CANE1
ATG8 + CANE1ΔAIM5
ATG8 + CANE1ΔAIM4,5
W202
V205
F183
V186
M192
M189
c
Prey
Bait
ATG8x
EV A B C D E F G H I
EV
CANE1
CANE1ΔAIM4
CANE1ΔAIM5
CANE1ΔAIM4,5
CANE1ΔC-terminus
DDO (-LW)
TDO (-LWH)
TDO (-LWH)+ 3-AT
d
RFP
GFP
merge
CANE1-RFP
X
GFP-CANE1
CANE1-RFP
X
GFP-HDEL
e
RFP-ATG8B
GFP
RFP
ChlA
merge
GFP-CANE1
GFP-CANE1ΔAIM4
GFP-CANE1ΔAIM5
GFP-CANE1ΔAIM4,5
f
RFP-ATG8X
GFP-CANE1
GFP-CANE1ΔAIM4
GFP-CANE1ΔAIM5
GFP-CANE1ΔAIM4,5
RFP-ATG8A
RFP-ATG8B
RFP-ATG8C
RFP-ATG8D
RFP-ATG8E
RFP-ATG8F
RFP-ATG8G
RFP-ATG8H
RFP-ATG8I
α-RFP
α-GFP
TCE

Figure 4: CANE1 interacts with ATG8 isoforms via select AIMs. a, endogenous ATG8 interacts with CANE1. *In vivo* immunoprecipitation of extracts of Arabidopsis seedlings expressing CANE1-mCherry after germination on + Pi media for 5 days. ER stress was applied by incubation in +Pi with 5 µg/mL TM and 1 µM ConA containing liquid media for 7h. Input and bound proteins were visualized by immunoblotting with anti-RFP and anti-ATG8 antibodies, loading control Coomassie blue staining (CBB). **b**, Colabfold prediction of CANE1-ATG8 interaction via AIM4 and AIM5. *In silico* prediction of CANE1 interaction with ATG8E revealed interaction via AIM5 (stick representation; see also Figure S6) which locates in Arabidopsis ATG8E (surface representation–grey) AIM pockets, known as W-site (site 1 –yellow) and L-site (site 2 –slate blue) (top panel) interacting with W202 and V205 (top right panel, close view – red). *In silico* mutation of W202A and V205A (CANE1$^{\Delta AIM5}$) predicts ATG8E CANE1 interaction via AIM4 (middle panel, right close view –orange) with F183 and V186 interacting with site 1 and site 2 respectively. CANE1 depleted of AIM4 and AIM5 is not predicted to interact with ATG8E via the AIM pockets (lower row panels, CANE1 $^{\Delta AIM4/5}$ –green). **c**, CANE1 interacts AIM specific *in vivo*. Y2H assay between a GAL4 DNA binding domain (DBD, bait) fused variant of CANE1 with GAL4 activation domain (AD, prey) fused variants of all nine ATG8 isoforms A-I. GAL4-DBD and AD alone were included as negative controls (EV). The growth of yeast cultures on vector-selective (−Trp/−Leu) (top), interaction-selective (−Trp/−Leu/−His) (middle) and strong interaction-selective (−Trp/−Leu/−His + 3-aminotriazol) media (bottom) six days after spotting is shown. **d**, Subcellular localization of CANE1-RFP. Co-expression of CANE1-RFP with GFP-CANE1 (Upper row) or GFP-HDEL (lower row) in transient expression assays in *N. benthamiana*. The images are single optical sections of RFP (left column), GFP (center column) and merged signals (right column). Scale bars, 10 µm. **e**,**f** CANE1 interacts with ATG8 in an isoform and AIM specific manner. **e**, Localization of GFP-CANE1 variants (CANE1, CANE1$^{\Delta AIM4}$, CANE1$^{\Delta AIM5}$ CANE1$^{\Delta AIM4/5}$) transiently co-expressed with RFP-ATG8B in *N. benthamiana*. The images are single optical sections of GFP (first column), RFP (second column), chlorophyll A (third column, blue) and merged (including bright field) signals (last column). Scale bars, 30 µm, n = 3. **f**, *In vitro* co-immunoprecipitation assays of all nine RFP-ATG8x isoforms co-expressed with CANE1-GFP variants in *N. benthamiana* via RFP-Trap. Presence of RFP-ATG8A-I and GFP-CANE1 variants was visualized by immunoblotting with anti-RFP and anti-GFP antibodies, loading control TCE visualization, n = 5.

Figure 5

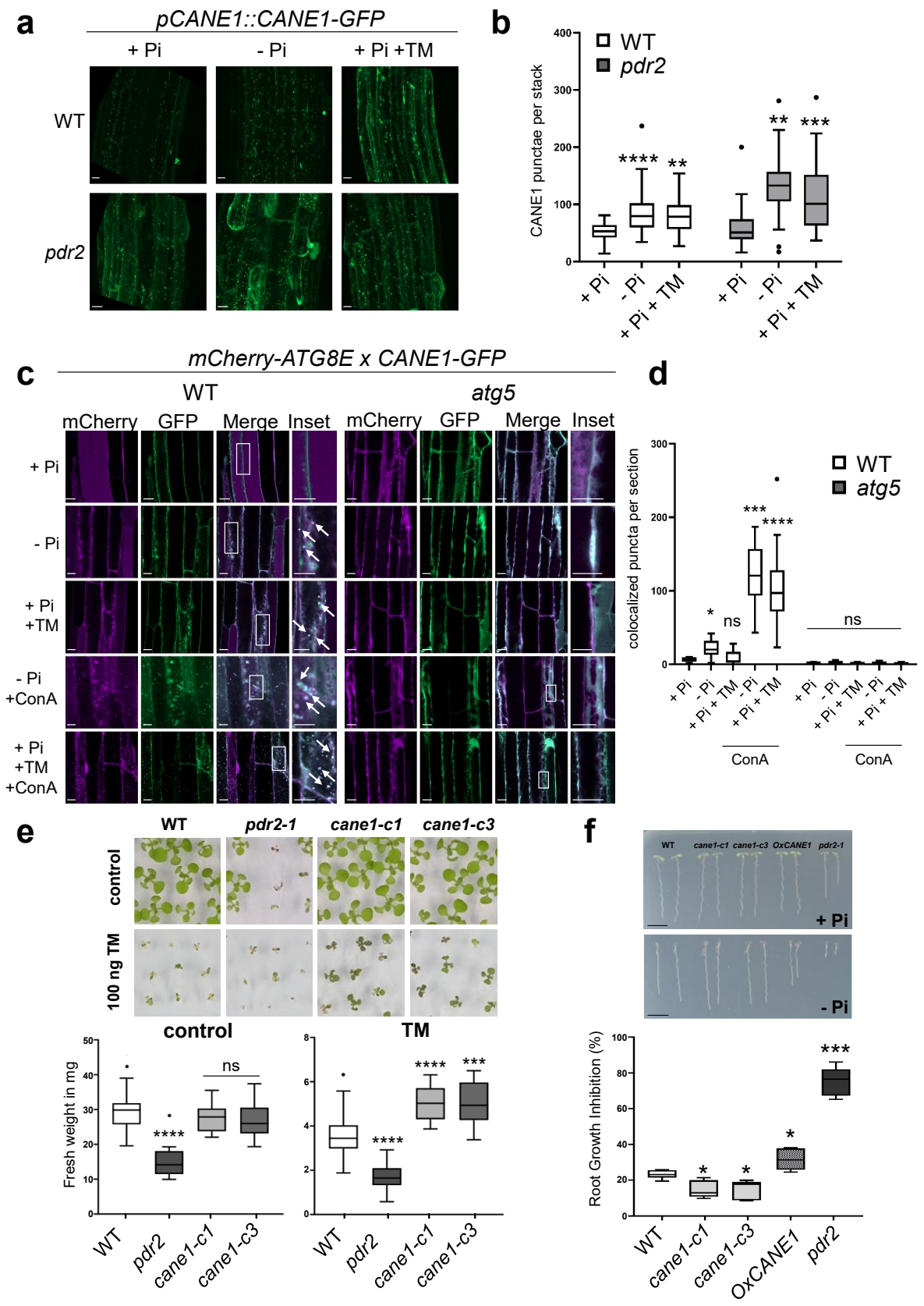
a
pCANE1::CANE1-GFP
+ Pi
- Pi
+ Pi +TM
WT
pdr2
b
WT
pdr2
CANE1 punctae per stack
+ Pi
- Pi
+ Pi + TM
c
mCherry-ATG8E x CANE1-GFP
WT
atg5
mCherry
GFP
Merge
Inset
+ Pi
- Pi
+ Pi +TM
- Pi +ConA
+ Pi +TM +ConA
d
WT
atg5
colocalized puncta per section
ns
ConA
e
WT
pdr2-1
cane1-c1
cane1-c3
control
100 ng TM
control
TM
Fresh weight in mg
ns
WT
pdr2
cane1-c1
cane1-c3
f
WT
cane1-c1
cane1-c3
OxCANE1
pdr2-1
+ Pi
- Pi
Root Growth Inhibition (%)
WT
cane1-c1
cane1-c3
OxCANE1
pdr2

Figure 5: CANE1 functions in Pi-dependent ER stress-induced autophagy. a, CANE1-GFP derived fluorescence in the transition zone of transgenic (*pCANE1::CANE1-GFP*) wildtype and *pdr2* seedlings after germination on +Pi agar (5 d) and subsequent transfer to + or –Pi medium for 24 h or treatment with TM in liquid + Pi media for 6 h. Shown are representative images from three independent experiments fused Z-stacks of the root tip. Scale bars, 20 µm. **b**, Quantification of CANE1-GFP puncta in root cells per area. Box plots show medians and interquartile ranges of detected autophagosomes; outliers (>1.53 interquartile range) are shown as black dots, n ≥ 34. Significant differences compared to wildtype are indicated with * when p value ≤ 0.05, ** when p value ≤ 0.01, *** when p value ≤ 0.001, and **** when p value ≤ 0.001. Unpaired t-test with Welch's correction. **c**, CANE1-GFP puncta colocalize with mCherry-ATG8E *in vivo*. Co-localization analyses of single plane confocal images obtained from transgenic wildtype (left panel) and *atg5* (right panel) Arabidopsis roots co-expressing mCherry-ATG8E (magenta) with CANE1-GFP (green). Seedlings were germinated 5 days prior transfer to the indicated treatment for 1 day (+/-Pi) or 5 h liquid media (+ Pi + TM; - Pi + ConA; + Pi + TM + ConA). Rectangles indicate Inset. Scale bars, 20 µm. **d**, Quantification of mCherry-ATG8E and CANE1-GFP colocalized puncta in the indicated treatments as described in a. n ≥ 5. **e-f**, loss of *CANE1* increases Arabidopsis ER stress tolerance. **e**, Top: 11 days old seedlings of wildtype, *pdr2*, *cane1-c1* and *cane1-c3* germinated on control or ER stress (100 ng/mL, TM) media. Bottom: Fresh weight of 5 pooled seedlings per sample, n = 17-18. **f**, Top: Germination of the indicated genotypes for eight days on Pi-sufficient (+Pi) or Pi-depleted (-Pi) conditions, scale bar = 1cm. Bottom: Primary root growth inhibition in percentage of the indicated genotypes, shown are summarized data of five independent biological experiments with each n ≥ 8. Significant differences compared to wildtype are indicated with * when p value ≤ 0.05, ** when p value ≤ 0.01, *** when p value ≤ 0.001, and **** when p value ≤ 0.001. Unpaired t-test with Welch's correction.

Figure 6

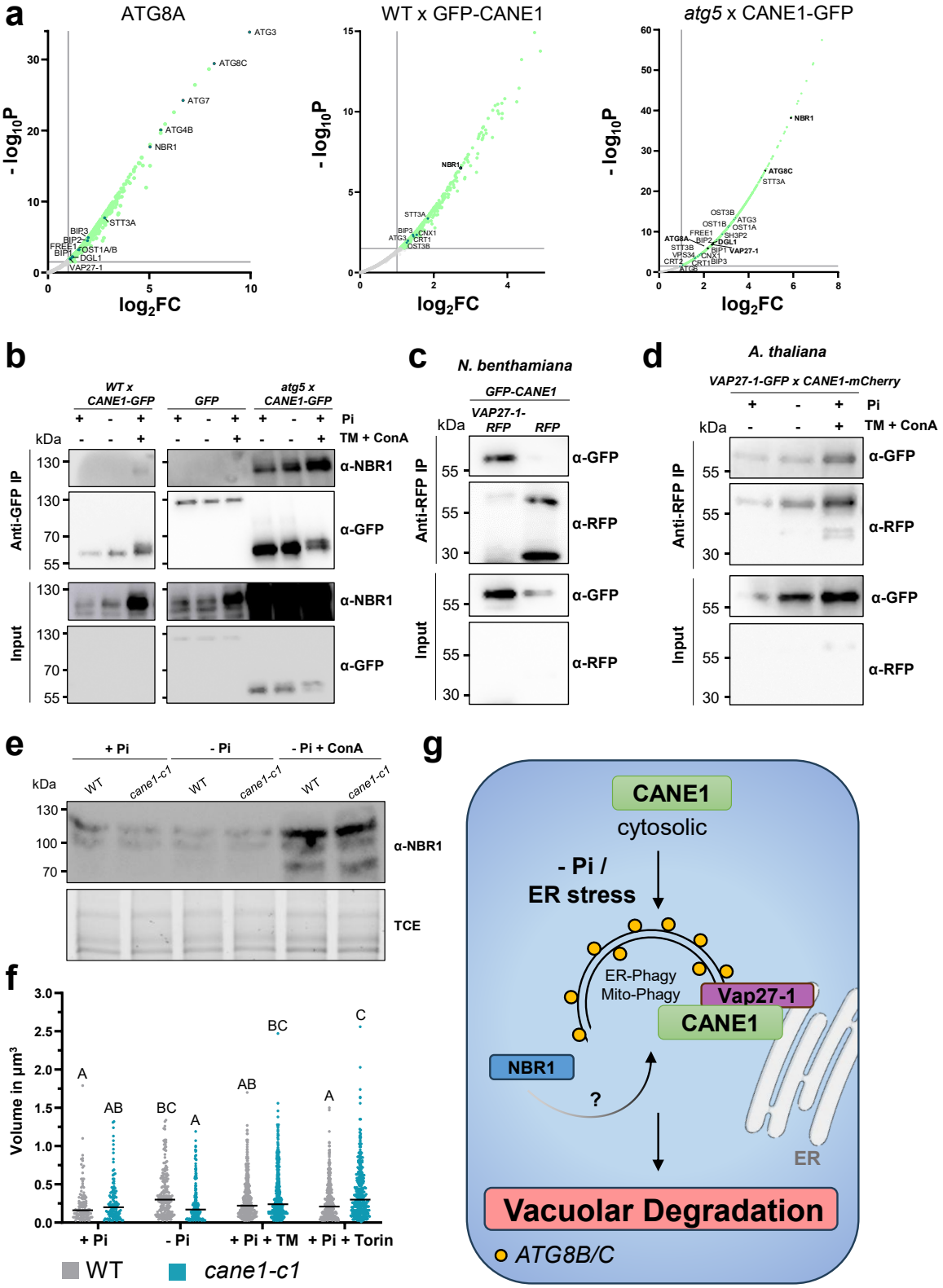
a
ATG8A
WT x GFP-CANE1
atg5 x CANE1-GFP
- log10P
log2FC
ATG3
ATG8C
ATG7
ATG4B
NBR1
STT3A
b
WT x CANE1-GFP
GFP
atg5 x CANE1-GFP
Pi
TM + ConA
kDa
Anti-GFP IP
Input
α-NBR1
α-GFP
c
N. benthamiana
GFP-CANE1
VAP27-1-RFP
RFP
Anti-RFP IP
α-GFP
α-RFP
d
A. thaliana
VAP27-1-GFP x CANE1-mCherry
e
+ Pi
- Pi
- Pi + ConA
WT
cane1-c1
α-NBR1
TCE
f
Volume in µm³
+ Pi
- Pi
+ Pi + TM
+ Pi + Torin
WT
cane1-c1
g
CANE1
cytosolic
- Pi /
ER stress
ER-Phagy
Mito-Phagy
Vap27-1
CANE1
NBR1
?
ER
Vacuolar Degradation
ATG8B/C

Figure 6: CANE1 interacts with NBR1 and VAP27-1 to modulate autophagosomal size. **a**, Enrichment of proteins interacting with ATG8A, *pUBQ10::GFP-CANE1* in wildtype and *pCANE1::CANE1-GFP* in *atg5* background in ER stress (+ TM + ConA) compared with a control expressing free GFP and represented by a volcano plot. Seedlings were germinated 10 days on liquid +Pi media prior to transfer to the indicated media. The horizontal grey line indicates the threshold above which proteins are enriched (P value <0.03, quasi-likelihood negative binomial generalized log-linear model), and the vertical dashed line indicates the threshold where the proteins' $\log_2$FC is greater than 1. **b**, Western blot analysis from immunoprecipitation (IP) experiments using wildtype and *atg5* expressing *pCANE1::CANE1–GFP* or *pCANE1::GFP-GUS* to immunoprecipitate NBR1. Seedlings were germinated 10 days on liquid +Pi media prior to transfer to + or – Pi for 24 h or ER stress treatment with 5 µg/ml TM and 1 µM ConA for 6 h. Whole roots were harvested. The blots were probed with anti-NBR1 and anti-GFP antibodies to detect the presence of NBR1. **c-d**, CANE1 interacts with VAP27;1 in *N.benthamiana* and *A. thaliana* roots in ER stress. **c**, IP of *p35S::VAP27-1-RFP* or *p35S::mCherry-HDEL* co-expressed with *pUBQ10::GFP-CANE1* in *N.benthamiana* leaves. Input and bound proteins were visualized with anti-GFP and anti-RFP antibodies. **d**, IP of extracts of F1 Arabidopsis roots co-expressing *p35S::CANE1-mCherry* and *pVAP27-1::VAP27-1-GFP* after transfer for 24 h to Pi sufficient or deficient liquid media. ER stress was applied by incubation in +Pi with 5 µg/ml TM and 1 µM ConA containing liquid media for 6 h. Input and bound proteins were visualized by immunoblotting with anti-RFP and anti-GFP antibodies. **e**, NBR1 protein amount is not influenced by CANE1 in Pi-deprived roots. Endogenous NBR1 detection by anti-NBR1 antibody in extracts from wildtype and *cane1-c1* roots germinated 5 days on +Pi media prior to transfer to +Pi, –Pi or –Pi containing 1 µM ConA liquid media for 24h. **f**, Loss of CANE1 affects autophagosome size in Pi-stressed roots. Seedlings of wildtype or *cane1-c1* expressing *p35S::GFP-ATG8A* were germinated for 5 days on +Pi media prior to transfer for 24 h to +Pi or –Pi media or incubated with 5 µg/ml TM or 1µM torin for 6 h for autophagic induction. Size of GFP-ATG8A labelled puncta were measured via Arivis software and calculated volume was plotted accordingly. Scatter plot, median is shown as bold line, letters denote statistical differences at $p < 0.05$ (Two-way ANOVA and Tukey's HSD post hoc test) and $n = 20$. **g**, Model of CANE1 function in autophagy. Induction of ER stress by local root tip Pi-sensing initiates CANE1 association to the ER and interaction with VAP27-1 to enable autophagosome maturation and membrane expansion for bulky cargo engulfment (e.g. ER-fractions, organelles). Potential NBR1 recruitment of CANE1 to the mature autophagosome by an unknown signal initiates ER-detachment and vacuolar degradation.

Supplementary Figure S1

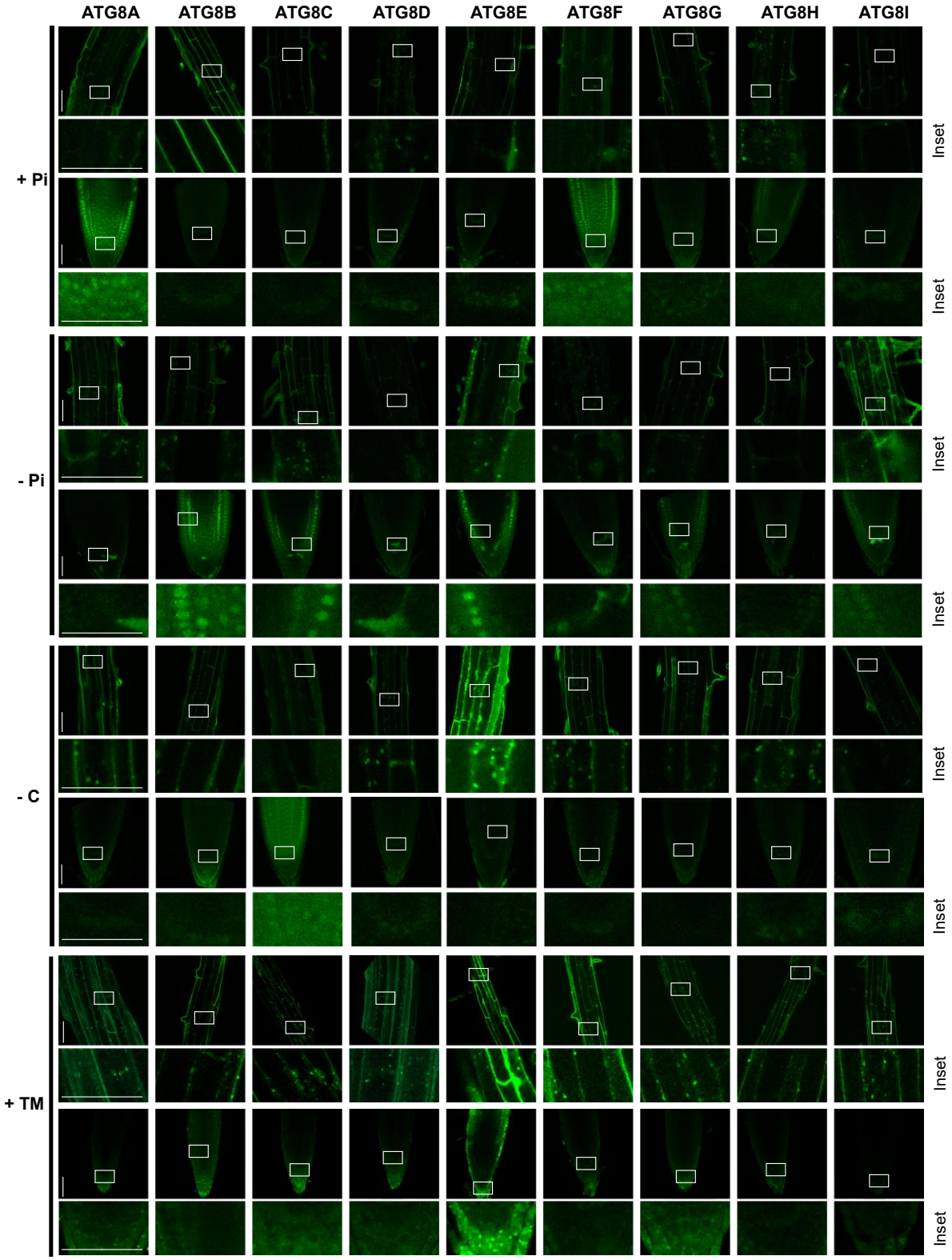

Supplementary Figure S1: Root tip ATG8 isoform specific autophagosome decoration. Seedlings were germinated 5 days prior transfer to the indicated treatment. Representative confocal microscopic images showing autophagosome formation of all 9 ATG8 isoforms (*pATG8x::GFP-ATG8x*) in the transition zone (row 1,3,5,7) or primary root tip (row 2,4,6,8) challenged with local Pi deprivation (row 3 and 4), carbon starvation (row 5 and 6) for 24 h or 5 µg/mL tunicamycin (TM) treatment (row 7 and 8) for 6-8 h, rectangle indicate Inset selection, $n \geq 10$.

Supplementary Figure S2

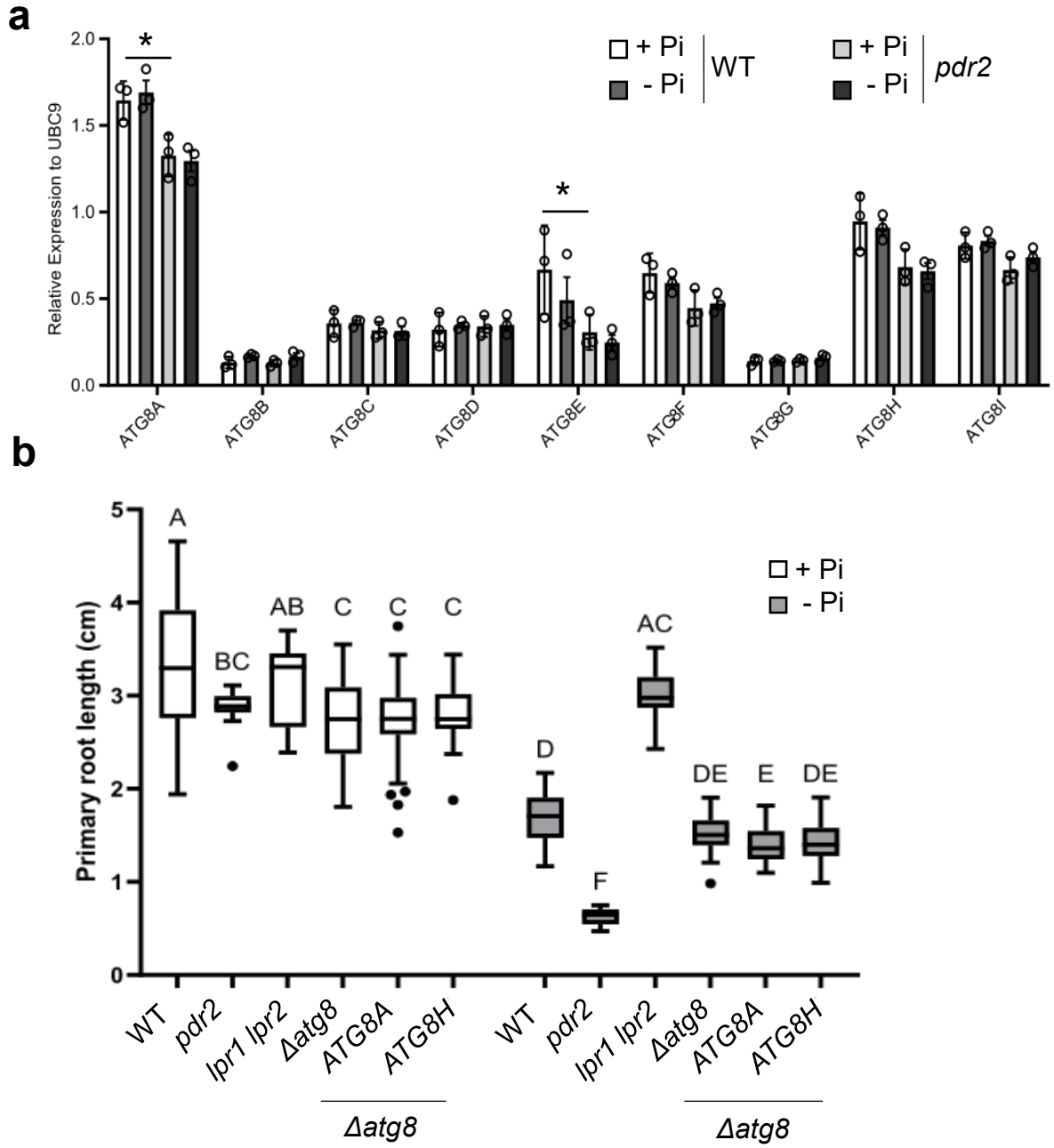

Supplementary Figure S2: Select ATG8 isoforms are involved in root tip Pi-dependent ER stress-mediated autophagy. a, Analysis of *ATG8A-I* relative transcript levels (normalized to UBC9 expression) in wildtype and *pdr2* root tips after transfer to +Pi or –Pi medium for 24 h (germinated for 5 days on +Pi) ±SD; n = 3; Two-way ANOVA, Post-hoc Tuckey, *p value ≤ 0.05. **b**, ATG8A and ATG8H fail to complement *Δatg8* sensitivity to Pi limitation. Seedlings were germinated for 5 days on +Pi media prior to transfer to medium supplemented with or without Pi (-Pi, +Pi) and imaged after 4 days. Gain of primary root extension was measured. Box plots show medians and interquartile ranges of primary root gain; outliers (>1.53 interquartile range) are shown as black dots. Letters denote statistical differences in condition at $p < 0.05$ (Two-way ANOVA and Tukey's HSD post hoc test) and $n \geq 13$-50.

Supplementary Figure S3

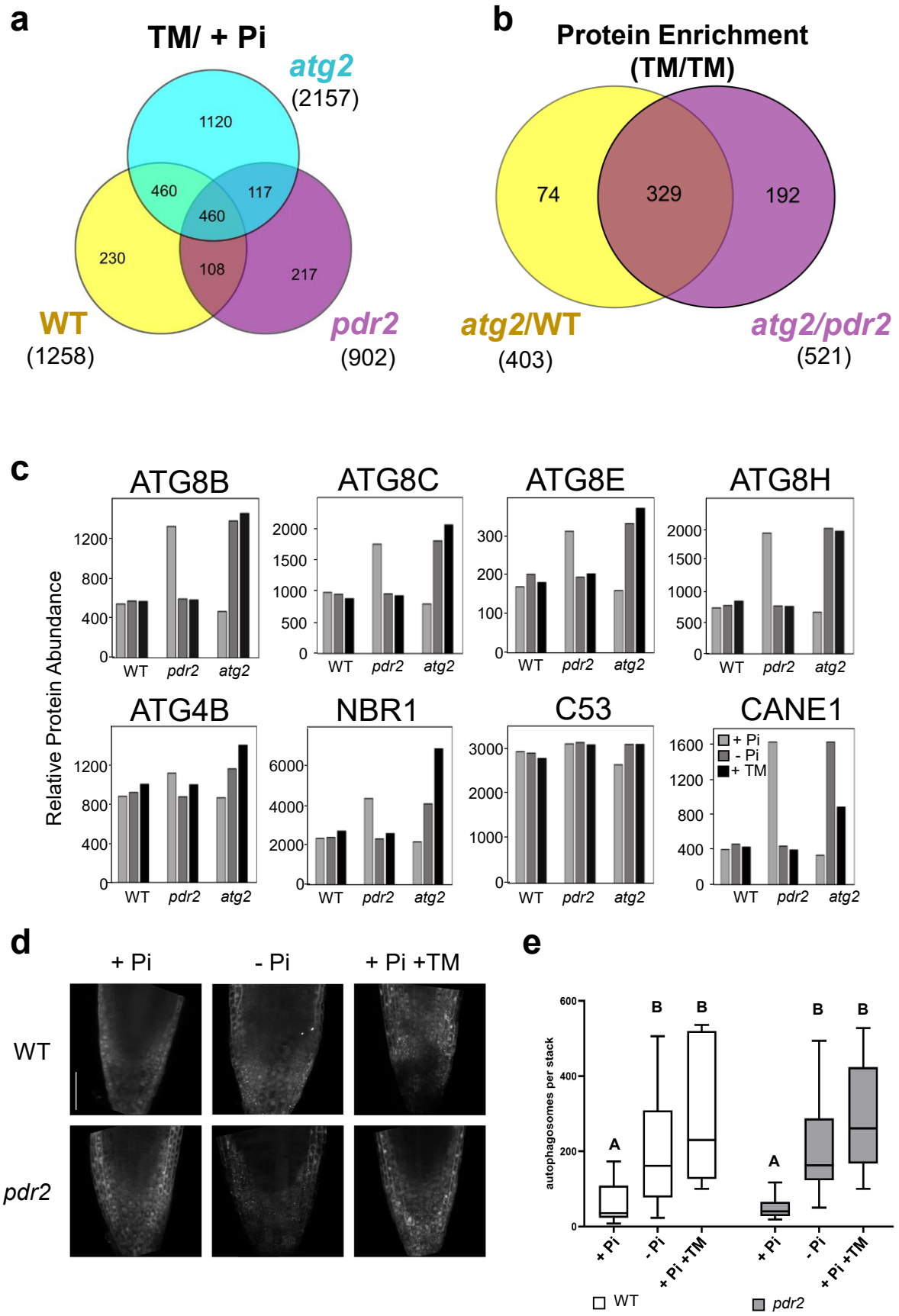

Supplementary Figure S3: ER-stress derived adaptation of root tip proteomes. a, Chemically induced ER stress impacts root proteome. Venn diagram of three overlapping pairwise comparisons for root tip TMT-MS conducted in wildtype (yellow), *pdr2* (magenta) and *atg2* (cyan) plants: wildtype (+Pi) vs wildtype (+Pi+TM) yellow cycle, *pdr2* (+Pi) vs. *pdr2* (+Pi+TM) magenta cycle, *atg2* (+Pi) vs. *atg2* (+Pi+TM) cyan cycle. Protein abundances with 0.6 > FC > 1.3. Total numbers are depicted in brackets. **b**, Overlap between proteins identified in + Pi + TM conditions enriched in *atg2* compared to wildtype (yellow) or *pdr2-1* (magenta) identified by quantitative MS, FC > 1.3. **c**, Proteins of the autophagic pathway are affected in local Pi-mediated root tip proteomic adaptation. Plotted protein abundances of ATG8B/C/E/H, ATG4B, NBR1, C53 and CANE1 in +Pi (light grey), -Pi (dark grey) and +Pi +TM (black) conditions measured via TMT-MS in wildtype, *pdr2* and *atg2*. **d,e** Autophagosome induction in Pi deprived and ER stressed root tips. **d**, GFP-ATG8A derived fluorescence in primary root tips of transgenic (*p35S::GFP-ATG8A*) wildtype and *pdr2* seedlings after germination on +Pi agar (5 d) and subsequent transfer to –Pi medium for 24 h or treatment with 5 µg/mL TM for 6 h. Shown are representative images from three independent experiments fused Z-stacks of the root tip. Scale bars, 50 µm. **e**, Quantification of GFP-ATG8 puncta in root cells per normalized area and number of slices. Box plots show medians and interquartile ranges of detected autophagosomes; outliers (>1.53 interquartile range) are shown as black dots. Letters denote statistical differences in condition at $p < 0.05$ (Two-way ANOVA and Tukey's HSD post hoc test) and $n \geq 6$.

Supplementary Figure S4

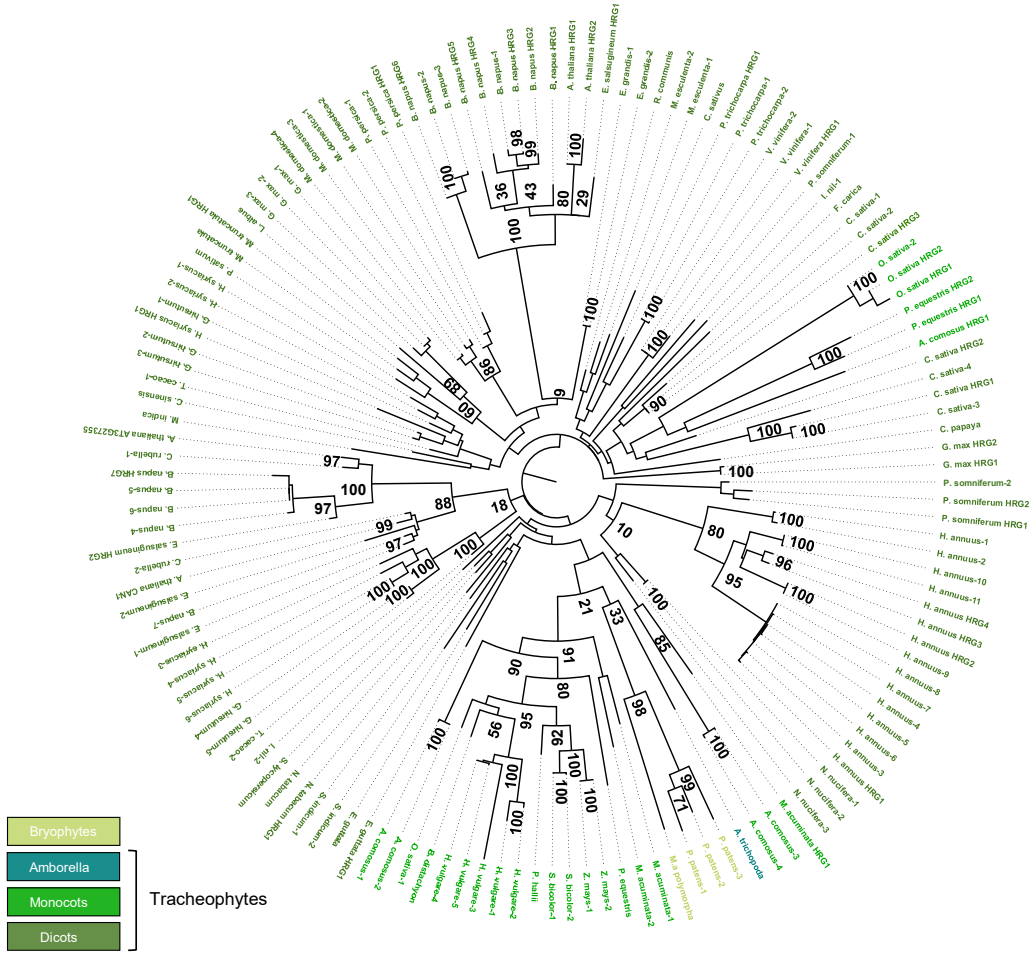

Supplementary Figure S4: CANE1 is present in most land plant species. Maximum-likelihood midpoint-rooted phylogenetic tree (250 bootstraps) of 139 predicted CANE1-like proteins (Phytozome). Identified CANE1 like proteins of bryophytes (light green), amborella (turquoise), monocots (leaf green) and dicots (dark green). Full-length CANE1-like sequences are annotated by organism in a numeric order, C-terminally truncated proteins are annotated according to *A. thaliana* HRG1 and 2 respectively.

Supplementary Figure S5

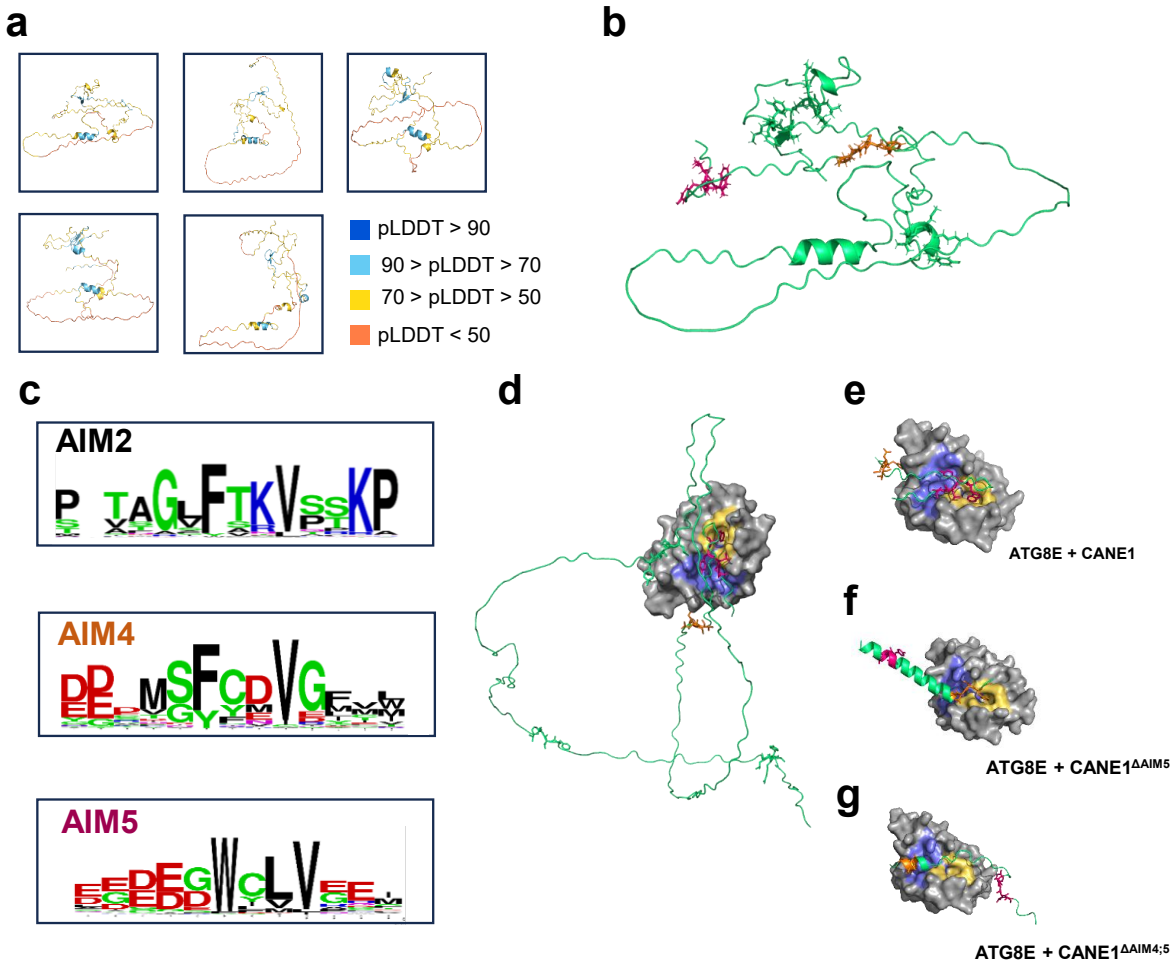

Supplementary Figure S5: CANE1 is an intrinsically disordered protein. Structure and interaction prediction of CANE1 by AlphaFold2. a, CANE1 is intrinsically disordered. Top five structure prediction by AlphaFold2 colored according to the pLDDT score of the predicted structure. **b**, CANE1 structure in green cartoon, with all five identified AIMs in stick representation (AIM1-3 green, AIM4 orange, AIM5 magenta). **c**, Specific conserved AIMs, with AIM4 and AIM5 exclusively present in full-length CANE1 proteins. **d-g** Predicted AIM-dependent interaction of full length CANE1 with ATG8E. **d**, CANE1 (cartoon, AA 192-210) interacts with ATG8E (surface representation) via AIM5 (stick, magenta), **e**, ATG8E AIM pockets, known as W-site (site 1 –yellow) and L-site (site 2 –slate blue) interacting with W202 and V205. **f**, Predicted interaction of CANE1$^{\Delta AIM5}$ (cartoon, AA 181-210) via AIM4 (stick, orange) and **g**, loss of predicted CANE1 ATG8E interaction in CANE1$^{\Delta AIM4,5}$ (cartoon, AA 181-210).

Supplementary Figure S6

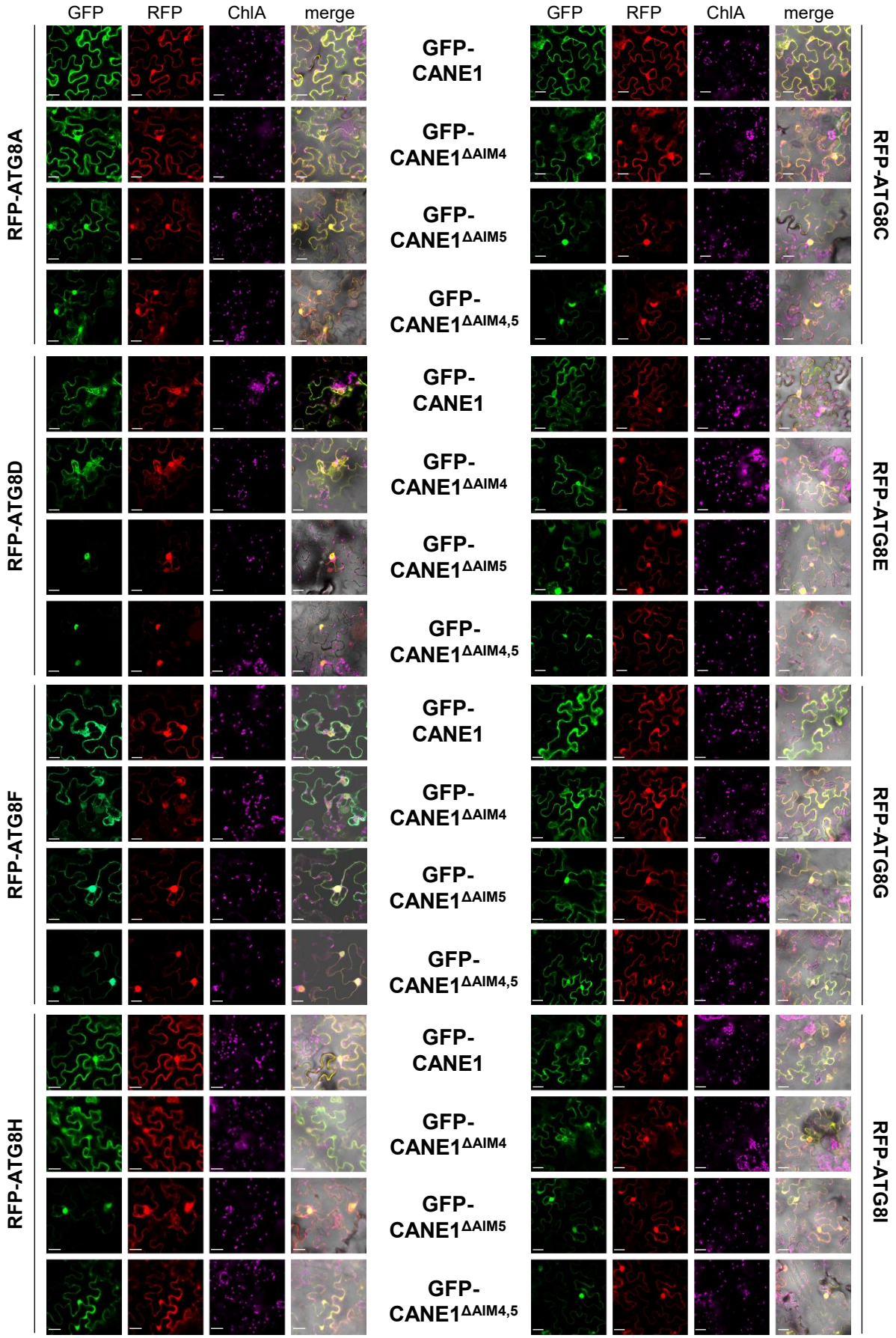

Supplementary Figure S6: CANE1 co-localizes with all ATG8 isoforms in *N. benthamiana*. Localization of GFP-CANE1 variants (CANE1, CANE1$^{\Delta AIM4}$, CANE1$^{\Delta AIM5}$ CANE1$^{\Delta AIM4/5}$) transiently co-expressed with RFP-ATG8A, C-I in *N. benthamiana*. The images are single optical sections of GFP (first column), RFP (second column), chlorophyll A (third column, blue) and merged (including bright field) signals (last column). Scale bars, 10 µm; n ≥ 3.

Supplementary Figure S7

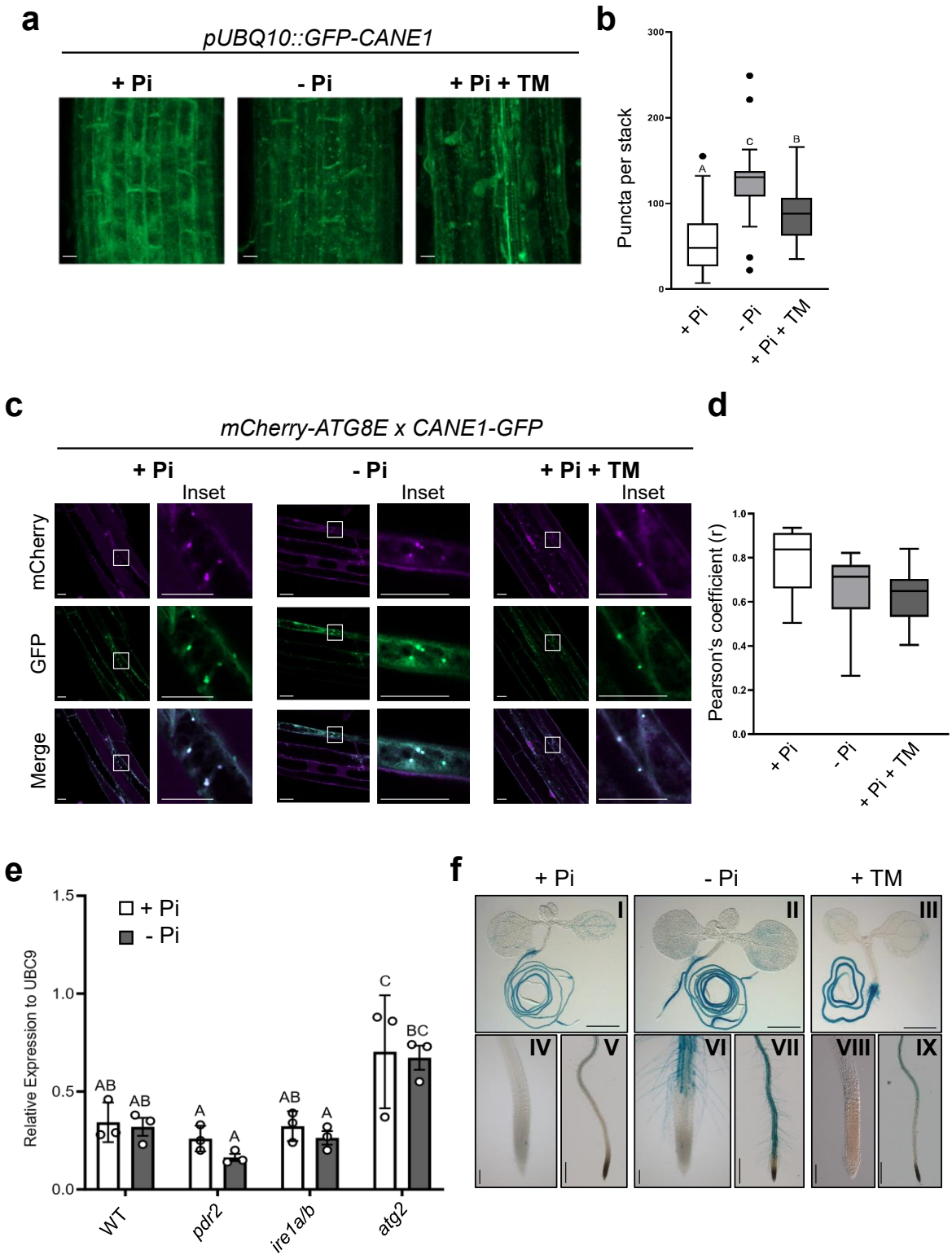

Supplementary Figure S7: CANE1 protein functions in ER stress-induced autophagy by local Pi sensing. a, GFP-CANE1 derived fluorescence in primary root tips of transgenic (*pUBQ10::GFP-CANE1*) wildtype seedlings after germination on +Pi agar (5 d) and subsequent transfer to –Pi medium for 0-24 h or treatment with 5 µg/mL TM for 6 h. Shown are representative images from three independent experiments fused Z-stacks of the transition zone. Scale bar 20 µm. **b**, Quantification of GFP-CANE1 puncta per stack in the indicated treatments. Box plots show medians and interquartile ranges of detected puncta; outliers (>1.53 interquartile range) are shown as black dots. Letters denote statistical differences in condition at $p < 0.05$ (Two-way ANOVA and Tukey's HSD post hoc test) and $n \geq 30$. **c**, CANE1-GFP puncta colocalize with mCherry-ATG8E *in vivo*. Co-localization analyses of single plane confocal images obtained from transgenic Arabidopsis roots co-expressing mCherry-ATG8E (magenta) with CANE1-GFP (green) in wildtype. Seedlings were germinated 5 days prior transfer to the indicated treatment for 1 day (+/-Pi) or 5 h (TM). Scale bars, 20 µm, $n \geq 10$. **d**, Pearson's Coefficient (r) analysis of the colocalization of CANE1-GFP and mCherry-ATG8E. Box plots show medians and interquartile ranges with five independent measures per biological replicate, $n \geq 10$. **e**, *CANE1* expression relative to UBC9 in gain of primary root tip 1 day after transfer of wildtype, *pdr2*, *ire1a/b* and *atg2.* Letters denote statistical differences in condition at $p < 0.05$ (Two-way ANOVA and Tukey's HSD post hoc test) and $n = 3$. **f**, *pCANE1::GUS* activity in 10 days old wildtype seedlings after transfer to the indicated media for two days or incubation with TM for 6 h, $n = 3$. Overview of the seedlings (I-III) scale bar 1 cm, primary root tip (IV-IX) with IV, VI, VIII scale bar 100 µm and V, VII, IX scale bar 1mm; $n \geq 6$.

Supplementary Figure S8

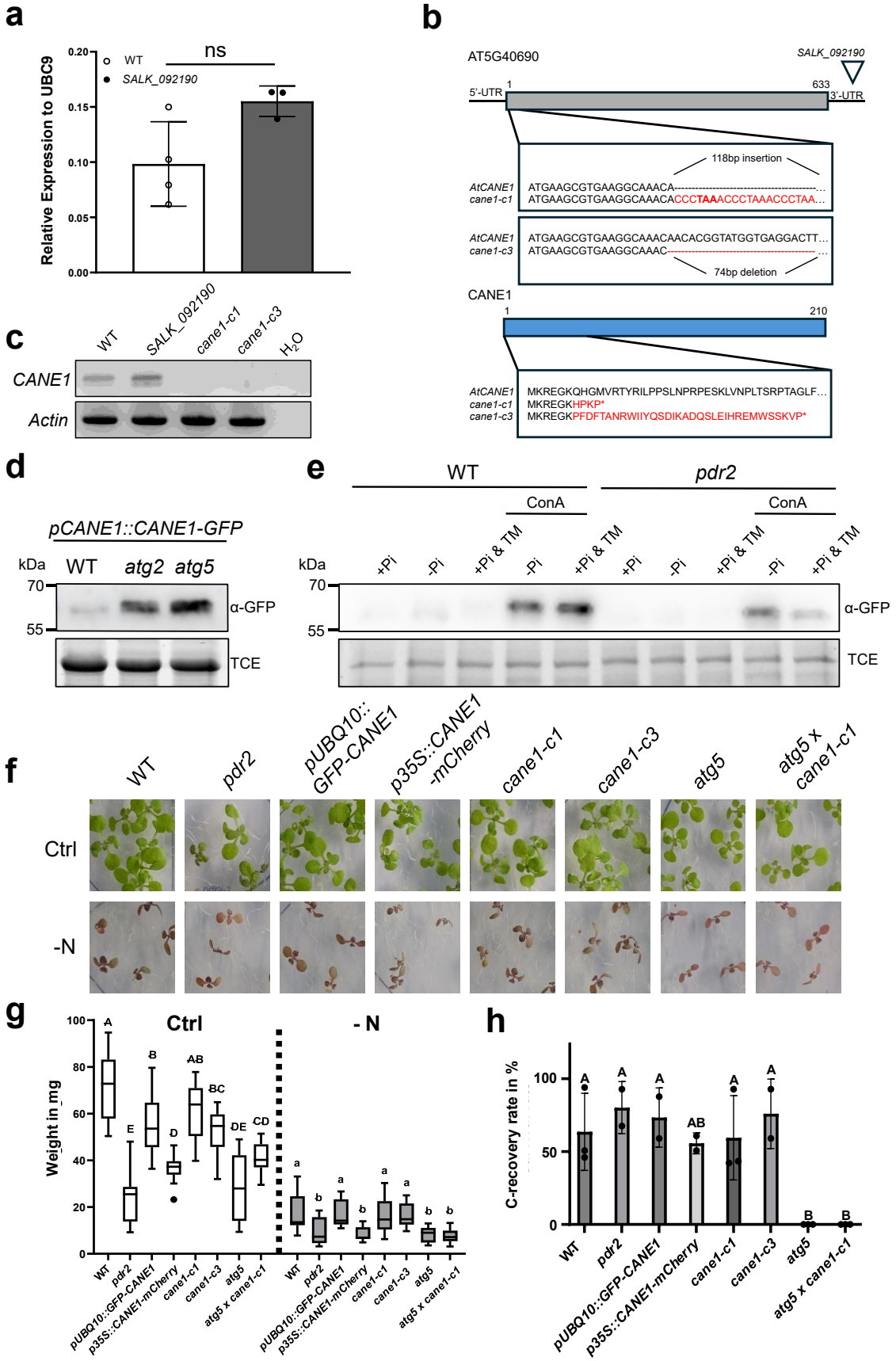

Supplementary Figure S8: CANE1 functions in ER stress-mediated autophagy. a, Transcriptional regulation of *CANE1* is not altered in SALK-Insertion line. Analysis of *CANE1* relative transcript level (normalized to UBC9 expression) of wildtype and *SALK_092190* insertion line seedlings (germinated for 5 days on +Pi media) ±SD; n ≥ 3; Students t-test. **b**, sequence analysis of *CANE1* (AT5G40690). Scheme of two *cane1* CRISPR mutants, *cane1-c1* and *cane1-c3*. Both mutants contain deletions/insertions where *cane1-c1* harbors a 118-bp insertion, while the *cane1-c3* mutant possesses a 74-bp deletion. The deletions/insertions lead to amino acids changes and premature stop codons in both mutants. **c**, Expression analysis of *CANE1* by semiquantitative RT-PCR by using cDNA isolated from wildtype, *SALK_092190*, *cane1-c1*, and *cane1-c3* seedlings. **d**, Amount of *pCANE1::CANE1-GFP* in wildtype, *atg2* and *atg5* seedlings (germinated for 5 days on +Pi media) were analyzed by Western Blot. TCE was used as loading control, n = 4. **e**, 5-day old seedlings expressing *pCANE1::CANE1-GFP* in wildtype and *pdr2* mutant were transferred to the indicated media for 24 h, TM (300 ng/µl) ConA (1µM). Whole roots were harvested and analyzed by immunoblot. TCE was used as loading control, n = 3. **f, g** 5 days-old seedlings of the indicated genotypes were grown on full (Ctrl) and N-depleted media for 7 days. **g**, Analysis of seedling weight after treatment. Box plots show medians and interquartile ranges of primary root gain. Letters denote statistical differences in treatment condition at $p < 0.05$ (One-way ANOVA and Tukey's HSD post hoc test) and n = 8-16. **h**, Loss-of *CANE1* does not rescue carbon starvation in *atg5* mutant plants. 5 days-old seedlings of the indicated genotypes were germinated on full media, prior to carbon starvation for 12 days, followed by recovery on full media for one week, ±SD; n = 3; One-way ANOVA, Post-hoc Tuckey, *p value ≤ 0.05.

Supplementary Figure 9

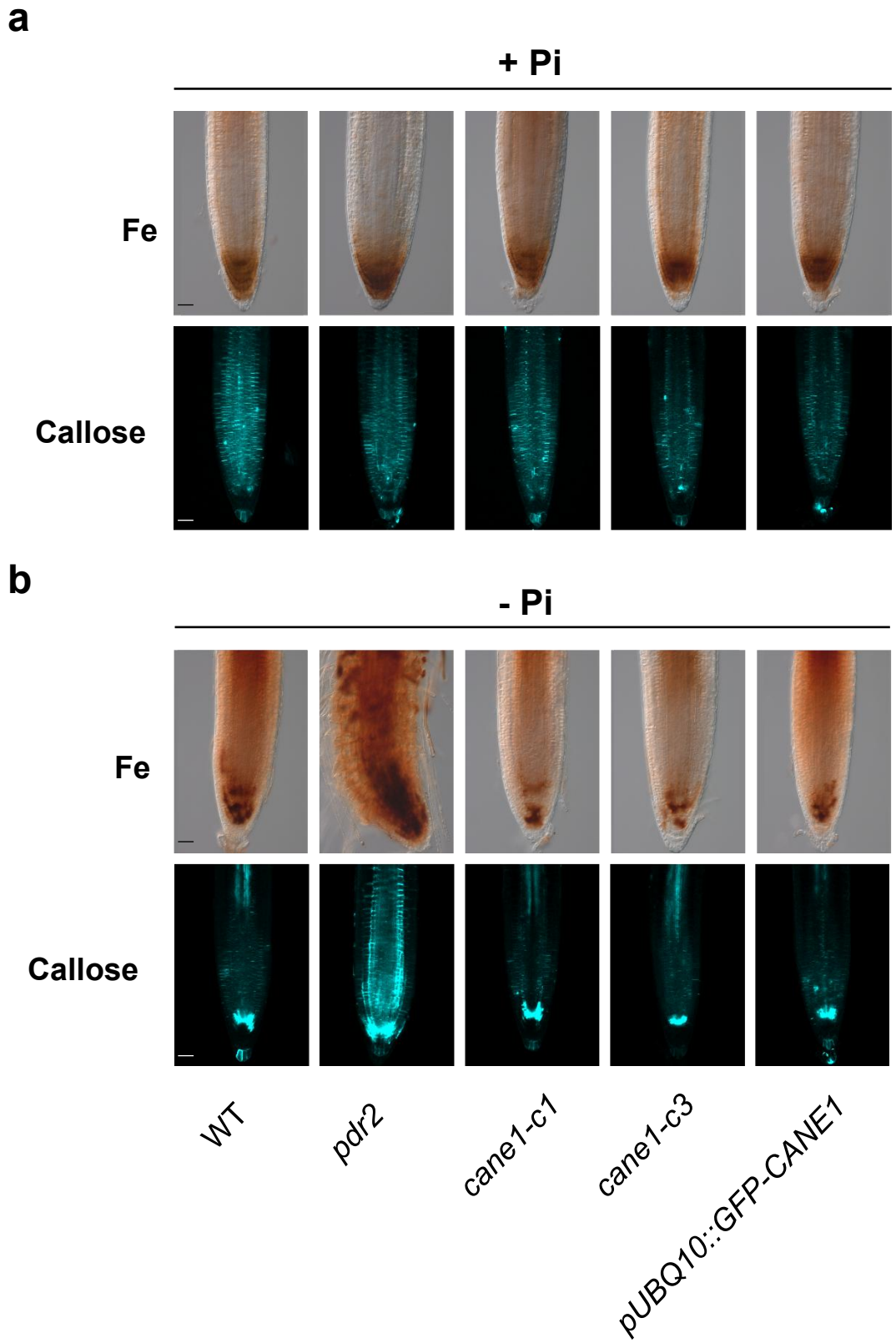

Supplementary Figure S9: LPR1-mediated local Pi response is not influenced by CANE1. a,b After germination (5 d, +Pi), seedlings were transferred to +Pi (**a**) or –Pi (**b**) medium (25 µM Fe). Top row: Three days after transfer, root tips of wildtype, *pdr2*, *cane1-c1*, *cane1-c3 and pUBQ10::GFP-CANE1* were monitored for Fe^{3+} accumulation by Perls staining coupled to diaminobenzidine (DAB) intensification. Bottom row: One day after transfer, root tips were monitored for callose deposition by aniline blue staining. Shown are representative images ($n \geq 20$). Scale bars 50 µm.

Supplementary Figure S10

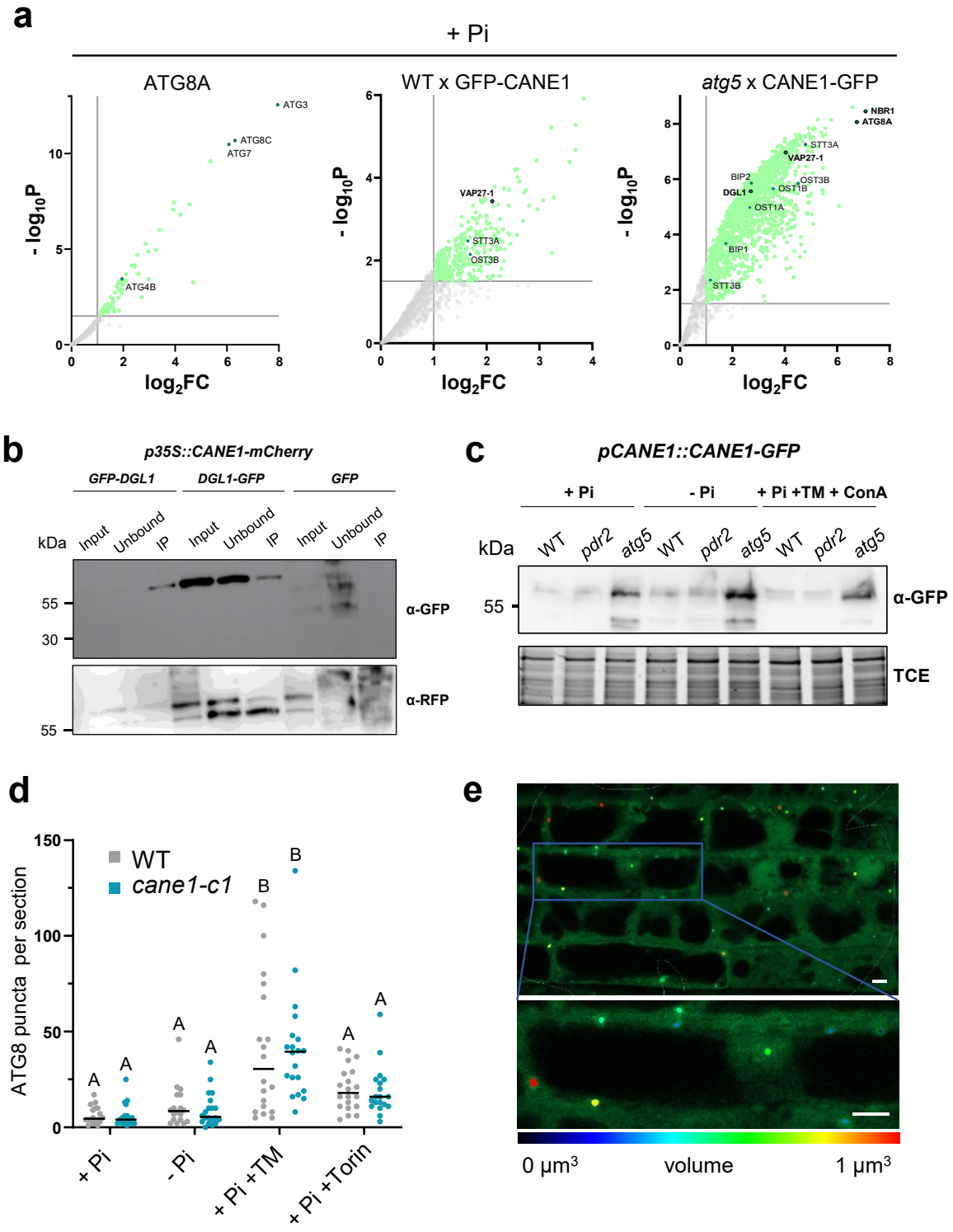

Supplementary Figure S10: CANE1 intersects with the autophagic pathway in ER stress. a, Enrichment of proteins interacting with *p35S::GFP-ATG8A*, *pUBQ10::GFP-CANE1* in wildtype and *pCANE1::CANE1-GFP* in *atg5* background in + Pi compared with a control expressing free GFP and represented by a volcano plot. The horizontal grey line indicates the threshold above which proteins are enriched (P value <0.03, quasi-likelihood negative binomial generalized log-linear model), and the vertical dashed line indicates the threshold where the proteins' $\log_2$FC is > 1. **b**, Western blot analysis from immunoprecipitation (IP) experiments of tobacco leaves co-infiltrated with *p35S::CANE1–mCherry* together with *p35S::DGL1-GFP*, *pUBQ10::GFP-DGL1* or *p35S::GFP-HDEL.* Input and bound proteins were visualized with anti-GFP and anti-RFP antibodies, n = 3. **c**, Amount of *pCANE1::CANE1-GFP* in wildtype, *pdr2* and *atg5* roots were analyzed by immunoblot. Seedlings were germinated 5 days on +Pi prior to transfer to the indicated media for 24 h or ER stress treatment with 5 µg/ml TM and 1 µM ConA for 6 h. TCE was used as loading control, n = 4. **d**, Autophagosome quantification in roots of wildtype and *cane1-c1* expressing *p35S::GFP-ATG8A.* Seedlings were germinated for 5 days on +Pi media prior to transfer for 24 h to +Pi or –Pi media or incubated with 5 µg/ml TM or 1µM torin for 6 h for autophagic induction. Scatter plot, median is shown as bold line, letters denote statistical differences at $p < 0.05$ (Two-way ANOVA and Tukey's HSD post hoc test), $n \geq 18$. **e**, Representative image of autophagosome volume quantification in Arivis. *p35S::GFP-ATG8A in* wildtype 24 h post transfer to –Pi is shown. Scale = 5 µm. Color-coded autophagosome volume according to the scale.